## Numerical study on instability and interaction of wind turbine wakes

by

Sasan Sarmast

August 2014 Technical Reports from Royal Institute of Technology Department of Mechanics SE-100 44 Stockholm, Sweden Akademisk avhandling som med tillstånd av Kungliga Tekniska Högskolan i Stockholm framlägges till offentlig granskning för avläggande av teknologie doktorexamen fredagen den 31 October 2014 kl<br/> 10.15 i sal F3, Kungliga Tekniska Högskolan, Lindstedtsvägen 26, Stockholm. Universitetsservice US-AB, Stockholm 2014

## Numerisk undersökning om instabilitet och interaktion av vindkraftverk vaknar

Sasan Sarmast Linné Flow Centre, KTH Mekanik, Kungliga Tekniska Högskolan SE-100 44 Stockholm, Sverige

#### Sammanfattning

Numeriska simuleringar utförs med hjälp av Navier-Stokes ekvationer för att nå en bättre förståelse av hur vakar genereras av vindkraftverk. Simuleringarna utförs genom att kombinera beräkningar med en CFD-metod (Computational Fluid Dynamics) med en actuator line metod, där bladen är representerade av volymskrafter.

I ett första steg i detta projekt genomfördes en numerisk studie som fokuserade på den instabilitet som resulterar i nedbrytning av de spetsvirvlar som skapas av turbinbladen. För att bestämma vilken frekvens som resulterade i störst instabilitet infördes störningar med låg amplitud nära spetsen på turbinbladen. Två grundläggande strömningsfall studerades; ett symmetriskt och ett asymmetriskt. I det symmetriska fallet användes en 120 graders symmetri och i det asymmetriska fallet användes en 360 graders domän. I det symmetriska fallet var de införda störningarna korrelerade, i det asymmetriska fallet infördes störningarna oberoende av varandra. Båda fallen analyseras med Proper Orthogonal Decomposition (POD) och Dynamic Mode Decomposition (DMD). Genom att analysera de dominerande moderna fann vi i det symmetriska fallet att tillväxten av instabilitet beror på frekvensen, i det asymmetriska fallet fann vi dock att nästan alla moder är involverade i spetsvirvelns destabilisering. Huvudsakligen beror spetsvirvelns instabilitet, och därmed även vaklängden, på de moder som resulterar i att virvelspiraler närmar sig varandra och resulterar i virvelparning. Vidare, genom att använda den ickedimensionella tillväxthastigheten, har man funnit att instabiliteten har en konstant tillväxttakt motsvarande  $\pi/2$ . Med hjälp av detta förhållande, och antagandet att turbulens intensiteten genererar en virvel med tillräcklig tillväxt, ger vi en analytisk relation för att bestämma längden på vaken, d.v.s. innan den blir instabil och bryts samman. Detta uttryck visar att vaklängden är omvänt proportionell mot kraften genererad av vindturbinen (thrust force), löptal och logaritmen av turbulensintensiteten.

I andra delen av studien utfördes LES-simuleringar (Large Eddy Simulation) med hjälp av Navier-Stokes ekvationer för att undersöka interaktion mellan turbiner. Tidigare actuator line simuleringar, på en enskild turbin, visar att noggrannheten i resultaten är direkt relaterad till kvaliteten på bladdata. Därför utfördes en serie av experiment på tvådimensionella bladprofiler,

NREL S826, för att erhålla bladdata med hög kvalitet för låga Reynolds tal. De uppmätta resultaten användes för att beräkna rotorprestandan. Resultaten visade att prestanda samt vakutvecklingen bakom rotorn beräknas med hög noggrannhet. Det fanns dock vissa svårigheter att förutsäga kraften genererad av turbinen (thrust force). Vidare användes den nya bladdatan för att betrakta interaktion mellan två turbiner placerade i en linje samt placerade med en halv rotordiameters offset i sidled. De numeriska beräkningarna visar att man kan förutse rotorprestanda samt strömningen runt turbinerna med tillförlitlig noggrannhet och därmed att det är ett bra verktyg för undersökning av vindturbiners vindvaknar.

I det sista delprojektet genomfördes en utvärdering av prestanda och strukturer i vaken nära turbinen. En analytisk virvelmodell presenteras. Modellen bygger på att konstant cirkulation längs bladen antas. Modellen förutsäger geometrin hos spetsvirveln bakom rotorn och tillåter att vaken fritt expanderar samtidigt som den lokala spetsvirvelns vinkel ändras. Två olika vindkraftverk har simulerats: ett vindkraftverk med konstant cirkulation längs bladet och ett andra med en mer realistisk cirkulationsfördelning, för att jämföra resultaten av virvelmodellen med realistiska turbinförhållanden. Virvelmodellen jämförs med actuator line beräkningar och jämförelsen visar att virvelmetoden kan approximera turbinprestandan för en turbin och kvalitativt beskriva strömningsfältet omkring turbinen med en försumbar beräkningsansträngning jämfört med CFD. Detta tyder på att virvelmodellen kan vara ett substitut för mer beräkningskrävande metoder för att studera vakars beteende under vissa förutsättningar.

**Deskriptorer:** vindkraftverk, vindvakar, CFD, actuator line metoden, virvelinstabilitet, vakar interaktion, reducerade modeller, POD, DMD, virvelmodell, virvelparning

## Numerical study on instability and interaction of wind turbine wakes

Sasan Sarmast

Linné Flow Centre, KTH Mechanics, Royal Institute of Technology SE-100 44 Stockholm, Sweden

#### Abstract

Numerical simulations of the Navier–Stokes equations are conducted to achieve a better understanding of the behavior of wakes generated by the wind turbines. The simulations are performed by combining the in-house developed code EllipSys3D with the actuator line technique.

In step one of the project, a numerical study is carried out focusing on the instability onset of the trailing tip vortices shed from a 3-bladed wind turbine. To determine the critical frequency, the wake is perturbed using low-amplitude excitations located near the tip spirals. Two basic flow cases are studied; symmetric and asymmetric setups. In the symmetric setup a 120° flow symmetry condition is dictated due to the confining the polar computational grid to  $120^{\circ}$ or introducing identical excitations. In the asymmetric setup, uncorrelated excitations are imposed near the tip of the blades. Both setups are analyzed using proper orthogonal decomposition (POD) and dynamic mode decomposition (DMD). By analysing the dominant modes, it was found that in the symmetric setup the amplification of specific waves (traveling structures) traveling along the tip vortex spirals is responsible for triggering the instability leading to wake breakdown, while by breaking the symmetry almost all the modes are involved in the tip vortex destabilization. The presence of unstable modes in the wake is related to the mutual inductance (vortex pairing) instability where there is an out-of-phase displacement of successive helix turns. Furthermore, using the non-dimensional growth rate, it is found that the mutual inductance instability has a universal growth rate equal to  $\pi/2$ . Using this relationship, and the assumption that breakdown to turbulence occurs once a vortex has experienced sufficient growth, an analytical relationship is provided for determining the length of the stable wake. This expression shows that the stable wake length is inversely proportional to thrust, tip speed ratio and the logarithmic of the turbulence intensity.

In second study, large eddy simulations of the Navier–Stokes equations are also performed to investigate the wake interaction. Previous actuator line simulations on the single model wind turbine show that the accuracy of the results is directly related to the quality of the input airfoil characteristics. Therefore, a series of experiments on a 2D wing are conducted to obtain high quality airfoil characteristics for the NREL S826 at low Reynolds numbers. The new measured data are used to compute the rotor performance. The results show that the power performance as well as the wake development behind the rotor are well-captured. There are, however, some difficulties in prediction

of the thrust coefficients. The continuation of this work considers the wake interaction investigations of two turbines inline (full-wake interaction) and two turbines with spanwise offset (half wake interaction). It is demonstrated that the numerical computations are able to predict the rotor performances as well as the flow field around the model rotors, and it can be a suitable tool for investigation of the wind turbine wakes.

In the last study, an evaluation of the performance and near-wake structure of an analytical vortex model is presented. The vortex model is based on the constant circulation along the blades (Joukowsky rotor) and it is able to determine the geometry of the tip vortex filament in the rotor wake, allowing the free wake expansion and changing the local tip vortex pitch. Two different wind turbines have been simulated: a wind turbine with constant circulation along the blade and the other setup with a realistic circulation distribution, to compare the outcomes of the vortex model with real operative wind turbine conditions. The vortex model is compared with the actuator line approach and the presented comparisons show that the vortex method is able to approximate the single rotor performance and qualitatively describe the flow field around the wind turbine but with a negligible computational effort. This suggests that the vortex model can be a substitute of more computationally-demanding methods like actuator line technique to study the near-wake behavior.

**Descriptors:** wind turbine, wakes, CFD, actuator line method, vortex instability, wake interaction, model reduction, POD, DMD, vortex model, vortex pairing

#### Preface

A brief introduction on the basic concepts, methodologies and summary of the projects are presented in the first part. The second part contains six articles. The papers are adjusted to comply with the present thesis format for consistency, but their contents have not been altered as compared with their original counterparts.

#### List of appended papers

- Paper 1. S. SARMAST, R. DADFAR, R.F. MIKKELSEN, P. SCHLATTER, S. IVANELL, J.N. SØRENSEN & D.S. HENNINGSON, 2014 Mutual inductance instability of the tip vortices behind a wind turbine. *Journal of Fluid Mechanics* 755, pp. 705-731
- Paper 2. J.N. SØRENSEN, R.F. MIKKELSEN, D.S. HENNINGSON, S. IVANELL, S. SARMAST & S.J. ANDERSEN, 2014 Simulation of wind turbine wakes using the actuator line technique. *Submitted to Philosophical Transactions of The Royal Society A*
- Paper 3. S. Sarmast & R.F. Mikkelsen, 2013 The experimental results of the NREL S826 airfoil at low Reynolds numbers. Technical report
- **Paper 4.** S. Sarmast & R.F. Mikkelsen, 2014 Numerical study on the performance and the wake development of single and two in-line model wind turbines. *Technical report*
- Paper 5. S. Sarmast, H. Sarlak, S. Ivanell & R.F. Mikkelsen, 2014 Numerical investigation of the wake interaction between two model wind turbines with spanwise offset. *Journal of Physics: Conference series* **524** 012137 doi:10.1088/1742-6596/524/1/012137
- **Paper 6.** S. Sarmast, A. Segalini, S. Ivanell & R.F. Mikkelsen, 2014 Comparison of the near-wake between a simplified vortex model and actuator line simulations of a horizontal-axis wind turbine. *Submitted to Wind Energy*

#### Other papers

The following papers are not included in this thesis due to an overlap in content or a content going beyond the scope of this thesis.

Paper 1. S. Sarmast, P. Schlatter, S. Ivanell, R.F. Mikkelsen & D.S. Henningson, 2013

Instability of the helical tip vortices behind a single wind turbine. Wind energy - Impact of turbulence P. 165-174, Springer

Paper 2. J.N. SØRENSEN, R.F. MIKKELSEN, S. SARMAST, S. IVANELL, & D.S. HENNINGSON, 2014

Determination of wind turbine near-wake length based on stability analysis. Journal of Physics: Conference Series  $\bf 524$  012155 doi:10.1088/1742-6596/524/1/012155

**Paper 3.** R.F. MIKKELSEN, S. SARMAST, D.S. HENNINGSON & J.N. SØRENSEN, 2014

Rotor aerodynamic power limits at low tip speed ratio using CFD. Journal of Physics: Conference Series  $\bf 524$  012099 doi:10.1088/1742-6596/524/1/012099

Paper 4. H. Sarlak, S. Sarmast, J.N. Sørensen & R.F. Mikkelsen, 2014

Aerodynamic behaviour of NREL S826 airfoil at Re=100,000. *Journal of Physics: Conference Series* **524** 012027 doi:10.1088/1742-6596/524/1/012027

#### Division of work among authors

The main advisor for the project is Prof. Dan S. Henningson (DH). Dr. Robert F. Mikkelsen (RM) and Associate Prof. Stefan Ivanell (SI) are the co-advisors.

#### Paper 1

This work consists of large eddy simulations of the wind turbine wakes subjected to low amplitude perturbations. The amplification of the perturbations are analysed using two modal decomposition techniques, proper orthogonal decomposition and dynamic mode decomposition. The simulations were performed by Sasan Sarmast (SS) under the supervision of RM. The results were then analysed by SS, Reza Dadfar (RD) and Philipp Schlatter (PS). The manuscript was written by SS and RD with input from Jens N. Sørensen (JS), PS, RM, SI and DH.

#### Paper 2

This work demonstrates the utility of the actuator line technique to simulate and study the detailed flow characteristics behind wind turbines. The simulations were carried out by SS and Søren J. Andersen (SA). The results were then analysed by SS and SA. The manuscript was written by JS, SS and SA with the feedbacks from RM, DH and SI.

#### Paper 3

This work presents the performance characteristics of the NREL S826 airfoil for Reynolds numbers in a range of 40,000 to 120,000. The 2D airfoil was designed and manufactured by RM. The experiments were performed by SS under the supervision of RM. The manuscript was written by SS with the inputs from RM.

#### Paper 4

This work focuses on the numerical study on the performance and the wake development behind single and two in-line wind turbines. The simulations were carried out by SS under supervision of RM. The manuscript was written by SS with the inputs from RM.

#### Paper 5

This numerical study focuses on the wake interaction between two wind turbine with spanwise offset. Numerical simulations were performed by SS. The manuscript was written by SS with the feedbacks from Hamid Sarlak (HS), RM and SI.

#### Paper 6

This work focuses on evaluation of the performance and near-wake structure of an analytical vortex model. This project was initiated by SS and Antonio Segalini (AS). The computations were performed by SS and AS. The manuscript was written by SS and AS with the input from RM and SI.

### Contents

Abstra	act	iii
Prefac	e	vii
Part I		xiii
Chapt	er 1. Introduction	1
1.1.	Historical remarks	1
1.2.	World energy resources	2
1.3.	Wind energy: Today-Tomorrow	3
Chapt	er 2. Background	6
2.1.	Objective of the thesis	7
Chapt	er 3. Numerical modeling	9
3.1.	Flow solver, EllipSys3D	9
3.2.	Actuator line model	10
3.3.	Introducing and modelling the synthetic turbulence	12
3.4.	Wind turbines	13
Chapt	er 4. Flow analysis using modal decompositions	15
4.1.	Modal decomposition	15
4.2.	Proper Orthogonal Decomposition	16
4.3.	Dynamic Modal Decomposition	17
$\mathbf{Chapt}$	er 5. Stability of the tip vortices behind a wind turbine	20
$\mathbf{Chapt}$	er 6. Model for determining the stable wake length	25
Chapt	er 7. Interaction of wind turbine wakes	28
7.1.	Experimental investigation of the NREL S826 airfoil	28
7.2.	Setup A: Single model wind turbine	30
7.3.	Setup B: Two inline model wind turbines	33
7.4.	Setup C: Two model wind turbines with spanwise offset	35

Chapter	8. Near-wake comparison between ACL and vortex model	38	
Chapter 9	9. Conclusions	41	
Acknowledgments			
Bibliography			
Part II		47	
Paper 1.	Mutual inductance instability of the tip vortices behind a wind turbine	<b>d</b> 51	
Paper 2.	Simulation of wind turbine wakes using the actuator line technique	r 87	
Paper 3.	The experimental results of the NREL S826 airfoil a low Reynolds numbers	t 113	
Paper 4.	Numerical study on the performance and wake develop of a single and two inline model wind turbines	oment 129	
Paper 5.	Numerical investigation of the wake interaction between two model wind turbines with spanwise offset	e <b>n</b> 149	
Paper 6.	Comparison of the near-wake between actuator-line simulations and a simplified vortex model of a		
	horizontal-axis wind turbine	167	

# Part I Overview and summary

#### CHAPTER 1

#### Introduction

#### 1.1. Historical remarks

The existence of windmills dates back to more than 3000 years ago and they are the oldest device for extracting energy of wind on land (Sørensen 2011). There are records of the quite early utilisation of wind power for grinding grains. Even today as shown in figure 1.1, ruins of these vertical axis windmills that were running for centuries can be found in the border of Iran and Afghanistan (Golding 1976). The knowledge regarding the design and operation of windmills has been increased and many different types of windmills have been constructed since.

The first machine to produce electricity from the wind (wind turbine) was invented by Charles F. Brush in the United States in 1887. At the same time the Danish scientist Poul La Cour (1846-1908) undertook basic wind turbine research. Based on his inventions and development of the new rotors, in 1918 approximately 3% of the Danish electricity consumption was covered by wind

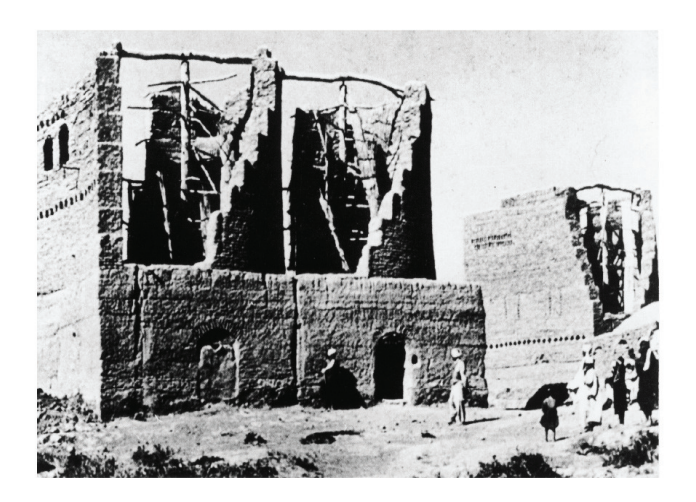


FIGURE 1.1. Ruins of a vertical axis windmill in the border of Iran and Afghanistan (Bennert & Werner 1989)

#### 2 1. INTRODUCTION

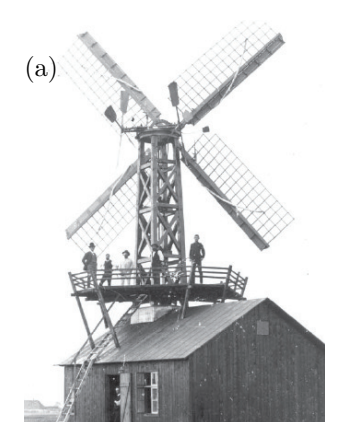






FIGURE 1.2. (a) The Poul la Cour first experimental wind turbine (1891) (b) The 200-kW Gedser turbine (1957). (c) A modern 2.5-MW wind turbine located in a cluster. The pictures are taken from Sørensen (2011).

turbines (Sørensen 2011). The research in wind energy has flourished and in a short period more and more efficient wind turbines were invented and successfully tested. Figure 1.2 shows Poul la Cour and a mid-1950s design of the wind turbine compared to the one with improved design. In mid-1970s, many countries such as United States, Germany, Great Britain, Sweden, the Netherlands, and Denmark launched national programs to investigate the potential of producing electricity from the wind and carried out big demonstration projects. With the effort of researchers, small industries and the national projects, the basis for the wind energy industry was formed.

#### 1.2. World energy resources

Current trends in energy consumption show an unsustainable path – economically, environmentally and socially. The current concerns about climate change relate strongly to the past technological developments, such as combustion of the fossil fuels. This dependency has given rise to a significant increase in the emissions of greenhouse gases out of which carbon dioxide is the most important. The energy-related greenhouse-gas emissions will be more than double by 2050, and security of supplies will be an issue in near future due to shortage of oil resources and an increased demand for oil (IEA 2013b). A solution to these problems can be substitution of fossil fuel resources with sustainable and low-carbon energy technologies. A closer look at the world energy supplies in figure 1.3(a) shows that the share of renewable energy resources such as hydro, geothermal solar, wind, bio-fuels and waste, and heat is relatively small compare to the non-renewable ones. A considerable part of the world resources are

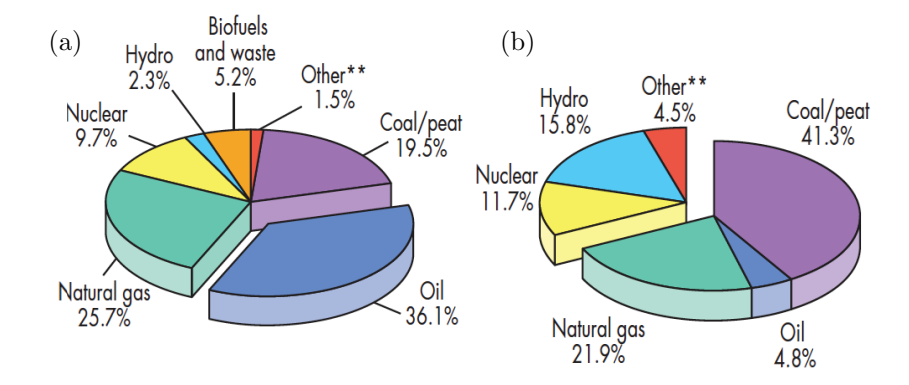


FIGURE 1.3. (a) Shares of the world energy supply. Other includes geothermal, solar, wind, heat, etc. The total energy supply is 5,239 Mtoe. IEA data from 2012. (b) Shares of the world electricity production. Other includes geothermal, solar, wind, bio-fules and waste, and heat. The total electricity produced is 22,126 TWh. IEA data from 2011. Source: IEA (2013a).

used to produce electricity resulting in an unwanted increase of  $CO_2$  emissions. The total produced electricity of the world is reported in figure 1.3(b) where the coal/peat and natural gas are the main contributors. Based on the latest statistics published in IEA (2013a), China produces one-third of its electricity from coal/peat resources and around one-fifth of the electricity in United States is produced from natural gas.

#### 1.3. Wind energy: Today-Tomorrow

Wind is the most advanced of the new renewable energy technologies which has attracted lots of attentions during the past decade. The development of wind power has been a successful story in the low-carbon technology as its capacity grows at almost 25% per year on average (see figure 1.4). Now many countries around the world have significant wind generating capacity; among those China, United States, Spain and Germany are the leaders. The statistics show that there are few countries such as Denmark, Portugal and Spain already provides almost 30%, 20% and 17% of their total electricity from wind energy resources, respectively (IEA 2013b). The technology keeps rapidly improving, and costs of electricity generation from land-based wind installations have continued to fall. Wind power is now being deployed in countries with good resources without special financial incentives.

The future development of wind energy requires larger and lighter wind turbines in order to reduce the cost and increase the energy production. Special

#### 4 1. INTRODUCTION

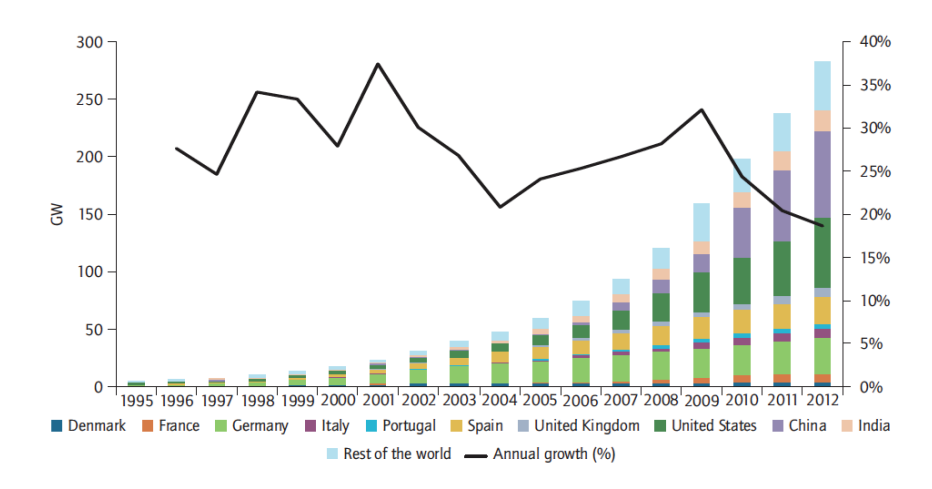


FIGURE 1.4. Global cumulative growth of wind power capacity, (IEA 2013b).

attention is paid towards placing the wind turbines in larger wind farms, cold climate, taking offshore wind farms to deeper waters and reallocating the wind turbines into more complex terrains. Advanced technologies are focused on rotors with larger swept area, resulting in greater energy capture, see figure 1.5. As the size of rotors increases, a detailed knowledge about the behaviour of wind turbines during operation is required for improved designs. In addition, noise reduction technologies become important specially for inshore wind farms. Today, state-of-the-art wind turbines have rotor diameters of up to 120 m and 5-MW installed power, and they are often placed in large wind farms with a production size corresponding to a nuclear power plant. So far, scaling up turbines which reduces the cost of wind energy has been effective, but it is not clear if this trend can continue forever.

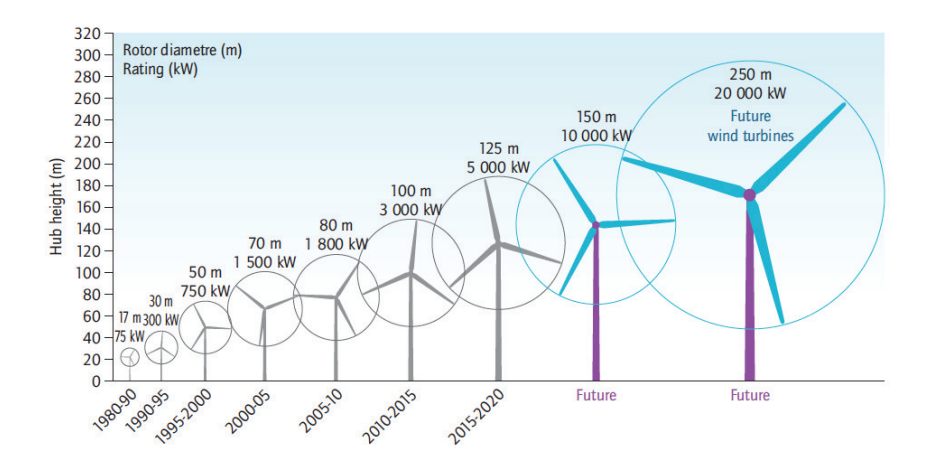


FIGURE 1.5. Growth in wind turbine size and prospects. data from adapted from EWEA 2009, (IEA 2013b).

#### CHAPTER 2

#### Background

The immediate flow behind wind turbines (or propellers) consists of a vortex sheet, which is formed by the lift distribution along the blades. Due to the interaction between the vortex elements a roll-up process occurs which results in forming of strong tip and distinct root vortices behind the rotor (Sørensen 2011). The area just behind the rotor is called near wake where the wake structure is directly linked to the rotor operating condition, characteristics and the incoming wind. The near wake is followed by far wake where the wake dynamics is no longer dependent on specific rotor characteristics instead it is more influenced by the surrounding environment, such as wakes from other turbines and the topography (Vermeer et al. 2003).

Wind turbines are often clustered in wind farms in order to minimize the overall installation and maintenance costs. Grouping of the wind turbines in such a way introduces two issues: the efficiency of the interior turbines decreases because of a lower incident wind speed and the life-time of the rotors shortens due to the increase of turbulence intensity inside wind farm. For example, Neustadter & Spera (1985) reported a reduction of 10% in power production for three turbines separated by 7 rotor diameters. Elliott (1991) reported power loss of 30-40% for the interior wind turbines in the full wake interaction condition; however, the averaged power loss is around 5-8% if different wind directions are considered. In general, it is estimated that the losses in energy production due to wake interference may vary from 5% to more than 15% depending on the wind farm layout (Smith et al. 1995). The increase in turbulence inside the wind farm is related to breakdown of the tip/root vortices shed from the rotor blades. In most situations, the tip/root vortex system is unstable and due to various instability mechanisms they breakdown and form small scale turbulent structures. It is important to note that if a wind turbine is located in a wake consisting of stable tip- and root-vortices the fatigue loading is more severe than in the case where the tip vortices have already broken down by instabilities (Sørensen 2011). Understanding the wake development and mechanisms leading to wake breakdown are, thus, important for the optimal design of a wind farm layout. Such an understanding can be obtained using experimental approaches and numerical simulation. The numerical simulations are preferred as compared to the experimental study for the wind farm optimization study. One reason is that the full scale experiments are very expensive and they are limited to only few global parameters while the numerical simulations can provide detailed information about the flow around the rotor. Another issue in full scale experiment is the variability in wind speed and turbulence intensity that makes the wake interaction study difficult. It should be noted that the numerical simulations also face some other difficulties such as accurate and reliable computations need access to massive computational resources and the rotation of the blade results in several problems in constructing a computational grid (Sanderse 2009).

#### 2.1. Objective of the thesis

The necessity of gathering wind turbines inside wind farms and wind farm optimization attracts attention of the scientists towards the detailed study on the wind turbine aerodynamics. Today, the aerodynamic research is moving towards "back to basic" approach as some of the fundamentals are far from being understood. Recently, the growth in computational resources offers new possibilities for detailed study on the wind turbine wakes.

The first objective of this project is to study the mechanism of tip vortex instability that leads to breakdown to turbulence. This study provides valuable information about the wake length for different operating condition of the wind turbine as well as the incoming wind turbulence. This knowledge is critical for correct placement of the turbine and their spacing inside a large wind farm.

In a wind farm, depending on the wind direction, the interior wind turbines operates fully or partially inside the wake of the upstream wind turbines. For wind farm optimisation, it is very important to rely on a prediction method/tool that can correctly obtain the basic physical behaviour of the wind turbine wakes. The objective of this study is to find a suitable method for simulating the flow field in wake interaction condition. This study provides information regarding the modelling limitations and how far the numerical methods can predict the performance and the interacting wake development.

Numerical computations of the wind turbine wakes are usually expensive and time consuming. Often there is a need for fast and reliable tool to give the first approximation about the wind turbine performance as well as flow field around the rotor. In this study, an evaluation of the performance and nearwake structure of an analytical vortex model is presented and it is investigated whether the predictions of this simplified and fast model can be a substitute of more expensive and time-consuming CFD approaches.

To reach these objectives, numerical studies on wind turbine wakes are carried out. The numerical model is based on large-eddy simulations (LES) of the Navier–Stokes equations using the actuator line method to simulate the wake behind the wind turbines. In the first study, two different modal decomposition technique are used to study the instability onset of the trailing tip vortices shed

#### 8 2. BACKGROUND

from the turbine blades. In the second study, first an experimental investigations are performed to obtain NREL S826 airfoil characteristics. Afterwards several computations are performed to study the wake interaction between wind turbines. In the last study the performance and near-wake development of a vortex model are compared with CFD computations.

The thesis is organised as follows: the first part provides a brief introduction to the concepts and tools included in the thesis. In chapter 1-2, background and motivation of the work are presented. The numerical procedures including simulation setups and actuator line method are reported in chapter 3. In chapter 4, a brief overview of the modal decomposition techniques is presented. A summary of the investigations are presented in chapters 5-8. Conclusions of the thesis are also presented in chapter 9. Second part of the thesis includes the articles where further detailed information is provided.

#### CHAPTER 3

#### Numerical modeling

This chapter presents the governing equations for a general flow solver together with the LES model and actuator line approach. Introduction of the synthetic turbulence to the computational domain and wind turbine specifications are also briefly discussed.

#### 3.1. Flow solver, EllipSys3D

Numerical computations are performed using a general 3D flow solver Ellip-Sys3D which is developed by collaboration between DTU (Michelsen 1992) and former Risø (Sørensen 1995). The code is based on a finite volume discretization of the incompressible Navier—Stokes equations in general curvilinear coordinates. The code is written in fortran 90 and it is parallelized using a message passing interface (MPI). EllipSys3D is formulated in primitive variables (pressure-velocity) in a non-staggered grid arrangement. In the present work, the pressure correction equation is solved using the SIMPLE algorithm and pressure decoupling is avoided using the Rhie/Chow interpolation technique. The convective terms are discretized using a hybrid scheme combining the third order accurate QUICK scheme and the fourth order CDS (Central Difference Scheme). This technique is employed as a compromise between unphysical numerical wiggles related to pure fourth-order CDS and numerical diffusion due to upwind biasing of the QUICK scheme.

Large eddy simulation (LES) is employed to model the small unresolved length scales of turbulence. LES applies a low-pass-filter on the Navier–Stokes equations, which results in a filtered velocity field. The velocity (U) is decomposed into a sum of filtered velocity  $(\overline{U})$  containing the large scales and the small scales (u') calculated using a sub-grid scale (SGS) model:

$$U = \overline{U} + u' \tag{3.1}$$

The flow field is then approximated by solving the filtered 3D incompressible Navier–Stokes equations for  $\overline{U}$ . The governing equations are then formulated as:

$$\frac{\partial \overline{U}}{\partial t} + \overline{U} \cdot \nabla \overline{U} = -\frac{1}{\rho} \nabla \overline{P} + \nabla [(\nu + \nu_{SGS}) \nabla \overline{U}] + \frac{1}{\rho} \mathbf{f}_{ext} \text{ and } \nabla \overline{U} = 0, \quad (3.2)$$

where  $\overline{U}$  is the filtered velocity,  $\overline{P}$  is the pressure,  $\rho$  is the density of air,  $f_{ext}$  represents the external body forces,  $\nu$  is the kinematic viscosity and  $\nu_{SGS}$  is the eddy viscosity. The body forces are introduced to account for modelling of the rotor (actuator line), atmospheric or synthetic turbulence, atmospheric boundary layer (if needed). In the present study, the sub-grid scale viscosity is modelled using the the mixed SGS model proposed by Ta Phuoc (1994). This SGS model is chosen as it has three advantages; it is simple, it accounts for the dissipation of energy, and at the same time it ensures the correct interaction between small resolved scales and large unresolved scales. In this model, the SGS viscosity is given by

$$\nu_{\text{SGS}}(\mathbf{x}, t) = \rho C_m |\nabla \times \overline{U}(\mathbf{x}, t)|^{\alpha} (q_c^2)^{\frac{1-\alpha}{2}} (\mathbf{x}, t) \overline{\Delta}^{1+\alpha}, \tag{3.3}$$

where  $\overline{\Delta}$  is the filter cut-off length and it is chosen to be  $(\Delta Vol)^{\frac{1}{3}}$ .  $\Delta Vol$  is the volume of a given computational cell.  $\mathbf{x}=(x_1,x_2,x_3)$  denotes the streamwise, lateral and vertical directions.  $\alpha$  and  $C_m$  are constants and they are set to 0.01 and 0.5, respectively. The kinetic energy  $q_c^2$  is evaluated as

$$q_c^2(\mathbf{x},t) = \frac{1}{2} (\overline{U} - \frac{\widetilde{U}}{U})(\overline{U} - \frac{\widetilde{U}}{U})$$
(3.4)

with  $\overline{\overline{U}}$  is double-filtered velocity and it represents the high frequency part of the resolved velocity field. The additional filter with tilde sign is referred to as the test filter and the size of test filter is twice as the size of the actual filter. For more information about EllipSys3D code and the LES modeling see Sagaut (2005); Ta Phuoc (1994) and Sørensen (1995).

#### 3.2. Actuator line model

The actuator line (ACL) method introduced by Sørensen & Shen (2002), is a fully three-dimensional and unsteady aerodynamic model for simulating the wind turbine wakes. The flow field around the wind turbine is governed by the three-dimensional incompressible Navier–Stokes equations while the influence of the rotating blades on the flow field is computed through body forces. The local forces on the blades are determined using a blade element approach combined with tabulated two-dimensional airfoil data. The forces are distributed radially along lines representing the blades of the wind turbine. Figure 3.1 shows a cross-sectional airfoil element at radius r. Here, the relative velocity  $U_{rel}$  is obtained as combination of the axial velocity  $U_0(1-a)$  and tangential velocity  $(1+a')\omega r$  at the rotor plane. a and a' are the axial and tangential induction factors. The axial induction factor is the fractional decrease in wind velocity between the freestream and the rotor plane. The induced tangential velocity in the rotor wake is specified through the tangential induction factor. The flow angle  $\phi$ , a combination of the local pitch  $\theta$  and angle of attacks  $\alpha$ , is

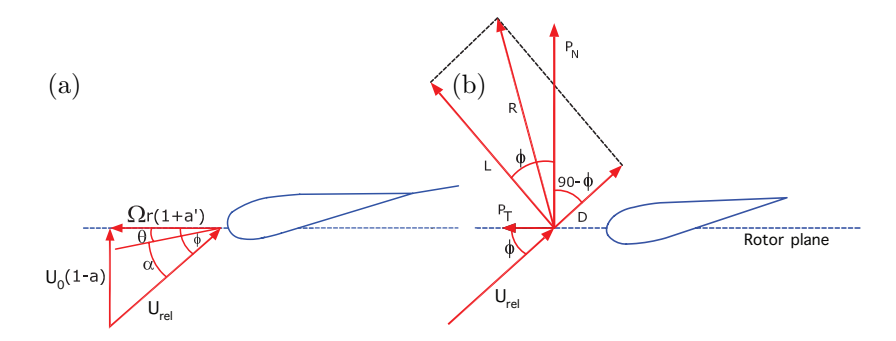


FIGURE 3.1. (a) Velocity and (b) force components acting on the airfoil element at radius r.

given by

$$tan(\phi) = \frac{(1-a)U_0}{(1+a')\omega r}. (3.5)$$

The aerodynamic forces acting on the airfoil are governed by the local velocities and determined from tabulated 2D airfoil data. Depending on the local angle of attack, the lift and drag forces reads

$$\mathbf{f}_{2D}^{n_B} = (\mathbf{L}, \mathbf{D}) = \frac{1}{2} \rho U_{rel}^2 c(C_L \mathbf{e}_L, C_D \mathbf{e}_D), \tag{3.6}$$

where c is the chord thickness,  $C_L(\alpha,Re_c)$  and  $C_D(\alpha,Re_c)$  are the lift and drag coefficients, respectively. These coefficients are function of the angle of attacks and the sectional Reynolds number. The directions of lift and drag forces are identified by the unit vectors  $\mathbf{e}_L$  and  $\mathbf{e}_D$ . The obtained forces are then smeared among neighbouring grid points in a two-dimensional Gaussian manner in order to avoid numerical singularity and mimicking the chord-wise pressure distribution. Here, the forces are distributed in the normal directions to each actuator line. This is done by taking the convolution of the computed load  $\mathbf{f}_{2D}^{n_B}$  and the regularization kernel  $\eta_\epsilon^{2D}$  as

$$\mathbf{f}_{\epsilon} = \mathbf{f}_{2D} \otimes \eta_{\epsilon}^{2D}, \quad \eta_{\epsilon}^{2D}(d) = \frac{1}{\epsilon^2 \pi} \exp\left[-\left(\frac{d}{\epsilon}\right)^2\right],$$
 (3.7)

where d is the distance between n-th point of the actuator line and a grid point in a plane normal to actuator line.  $\epsilon$  is the smearing parameter that serves to adjust the concentration of the regularized load.  $\epsilon$  is recommended to be in the order of  $1s < \epsilon < 4s$  where s is the size of a computational grid. For more details about the actuator line method and its implementation, see Mikkelsen (2003).

The main advantage of representing the blade as actuator line is that much fewer number of grid points are needed to obtain the fully resolved wake as compared to simulating the flow over actual geometry of the blade. Therefore, this model allows for the detailed study on the near-wake structure and the dynamics of the tip and root vortices. Another advantage of the actuator line model comes from simplicity in grid generation. In actuator line a simple structured grid is needed while lots of problems arise in connection with grid generation to resolve the actual geometry of the blade. The main drawback of actuator line approach is that the accuracy of the numerical computations depends on the quality of the tabulated airfoil data (Hansen *et al.* 2006).

#### 3.3. Introducing and modelling the synthetic turbulence

In computations, the wind tunnel turbulence is modelled by introducing the synthetic pre-generated turbulence fluctuations in a plane upstream of the wind turbines. The turbulence fluctuating velocities are imposed to the mean flow as body forces and they are computed from an algorithm proposed by Mann (1994, 1998).

The so-called Mann approach is based on modelling the spectral tensor derived from the linearization of the incompressible Navier–Stokes equations with an assumption of linear shear and a model for eddy life-time. The method can generate all three velocity components of a three-dimensional incompressible turbulence flow field, which is stationary, homogenous, Gaussian and anisotropic. In addition, this method is capable of simulating atmospheric turbulence with second order statistics. The output of the Mann algorithm is a three-dimensional box of turbulence which is equidistantly spaced. The generated box, has an axis parallel to the mean flow which is inferred as a time axis and it follows the Taylor's frozen turbulence hypothesis. After generating the frozen turbulence, the velocity fluctuations should be imposed as body forces in order to satisfy the continuity equation. Here, the magnitude of the body forces are computed as

$$\mathbf{f}_{fluc} = \dot{m}\mathbf{u} + \rho\epsilon_{turb}\frac{d\mathbf{u}}{dt},\tag{3.8}$$

where  $\dot{m}$  is the mass flux and  $\epsilon_{turb}$  is the regularization parameter. Similar to actuator line method, the forces are distributed in a Gaussian manner but only in one-dimension. Here the body forces are smeared perpendicular to the turbulent plane,

$$\mathbf{f}_{turb} = \mathbf{f}^{fluc} \otimes \eta_{\epsilon}^{1D}, \quad \eta_{\epsilon}^{1D}(d) = \frac{1}{\epsilon_{turb}\sqrt{\pi}} \exp\left[-\left(\frac{x - x_0}{\epsilon_{turb}}\right)^2\right],$$
 (3.9)

where  $x - x_0$  is the normalised distance between a grid point in the computational domain and point  $x_0$  on the turbulent plane. The  $\epsilon_{turb}$  is set equal to the grid size.

#### 3.4. Wind turbines

In the thesis, the computations presented are conducted using airfoil data from Tjæreborg wind turbine with NACA44xx profiles and NTNU modeled wind turbine with 14%-thick NREL S826 (Krogstad & Lund 2011).

The 2 MW Tjæreborg wind turbine is a three-bladed horizontal wind turbine with each blades consist of NACA44xx airfoil. The turbine has a blade diameter of D=61.12m and rotates at  $\Omega=22.1$  RPM, corresponding to the tip speed of 70.7m/s. The blade has a chord length of c=0.9m at the tip, increasing linearly to 3.3m at hub radius 6m. The blades are linearly twisted 1° per 3m. Figure 3.2 shows the lift and drag distributions of NACA 4412 and NACA 4424 airfoils. These profiles represent the airfoils used near the tip and root of the blade, respectively. Further technical details about the rotor can be found in Øye (1992).

The instability investigations are performed based on the Tjæreborg wind turbine operating at its optimum power condition ( $C_p = 0.49$ ) with a wind speed of 10m/s and tip speed ratio of 7.07. The Tjæreborg wind turbine is chosen to study the instability mechanism of the helical tip vortices due to its blade abrupt ending that results in a strong distinct tip vortices.

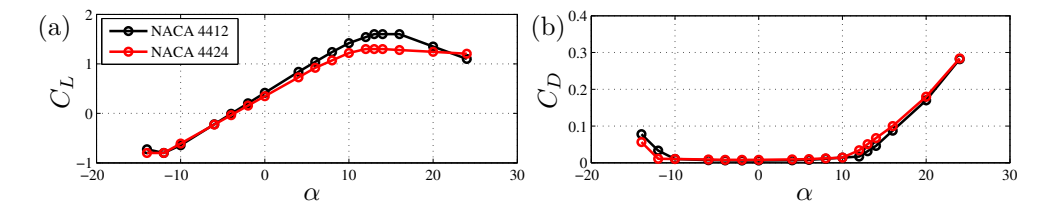


FIGURE 3.2. a) Lift and b) drag coefficients of NACA 4412 and NACA 4424 airfoils used in instability investigations. The Reynolds number is  $6\times10^6$ .

A rotor experiment has recently been carried out at NTNU using horizontal axis model scale rotors, for detailed investigation of the wake interaction. The modeled wind turbine is equipped with the 14% NREL S826 throughout the span. The family of the NREL S826 airfoils has been designed specially for the horizontal-axis wind turbines with the primary objectives of high maximum lift (maximum lift of at least 1.4), insensitivity to roughness, and low profile drag. In addition the airfoils should exhibit docile stalls. The blades are 44.25cm long and they have a chord length of 2.6cm at the tip increasing to 8.1cm near the root. The chord length is about three times wider than the commercial model turbines to reduce the Reynolds number effects. The blade is also twisted which has  $38^{\circ}$  pitch near the root which decreases to  $0^{\circ}$  near the tip. More information about the process of blade design and the performance of the airfoils at high

#### 14 3. NUMERICAL MODELING

Reynolds numbers  $(Re > 10^6)$  can be obtained from Pierella *et al.* (2012) and Somers (2005).

A measurement of the S826 airfoil is performed in order to get reliable airfoil characteristics at low Reynolds numbers ( $Re < 2 \times 10^5$ ). Figure 3.3 reports the measured lift and drag coefficients used for the wake interaction study.

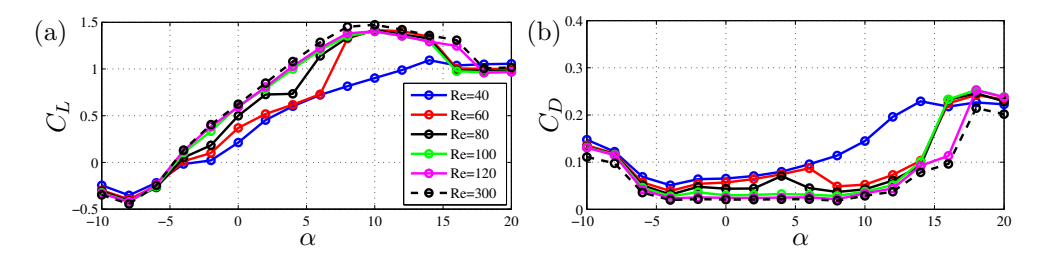


FIGURE 3.3. a) Lift and b) drag coefficients of NREL S826 airfoil used in the NTNU experiment. The reported Reynolds numbers are in  $10^3$ . The details of the experiment is presented in paper 3.

#### CHAPTER 4

#### Flow analysis using modal decompositions

The flow behind a wind turbine is complex and three-dimensional which means that it is difficult to directly extract the flow dynamics. The modal decomposition is an efficient way to identify the coherent structures and the stability properties of the flow. This chapter is focused on providing a brief theoretical background of two modal decomposition approaches: proper orthogonal decomposition (POD) (Lumley 1970; Sirovich 1987) and dynamic mode decomposition (DMD) (Rowley et al. 2009; Schmid 2010).

#### 4.1. Modal decomposition

The flow dynamics can be extracted from any given dataset obtained either from experiments or numerical simulations. Consider a dataset that contains velocity fields sampled equidistantly in time with spacing  $\Delta t$ . This datasequence with m descritized velocity fields  $\mathbf{u}_j = \mathbf{u}(\mathbf{x}_i, t_j) \in \mathbb{R}^n, t_j = j\Delta t, \ j = 0, 1, \dots, m-1$  is assembled columnwise into

$$\mathbf{U}_m = [\mathbf{u}_0, \mathbf{u}_1, \dots, \mathbf{u}_{m-1}] \in \mathbb{R}^{n \times m}, \tag{4.1}$$

where m is the number of snapshots and n is the total number of degree of freedom and is equivalent to the number of grid points multiplied by the number of velocity components. This number is usually large compared to the number of snapshots in the flow problem  $n \gg m$ . The modal decomposition approach splits the flow dynamics into space and time dependent parts by expanding the velocity field into spatial basis functions (the modes)  $\phi_k = \phi_k(x_i), k = 0, \dots, m-1$  and the corresponding temporal coefficients  $\mathbf{a}_k = \mathbf{a}_k(t_j)$ ,

$$\mathbf{u}(\boldsymbol{x}_i, t_j) = \sum_{k=0}^{m-1} \phi_k(\boldsymbol{x}_i) \mathbf{a}_k(t_j) \quad \forall j \quad \text{or} \quad \mathbf{U}_m = \mathbf{X}\mathbf{A}, \tag{4.2}$$

where the matrix **A** contains the temporal coefficients  $\mathbf{a}_k$  and **X** is the collection of the spatial basis (modes)  $\phi_k$ . Often only a few spatial structures describing the flow dynamics are important, and it is possible to obtain a low order approximation of the original flow field with a good accuracy using lower number of modes. In the following sections, two modal decomposition techniques of POD and DMD are presented for analysis of the wind turbine wakes.

#### 4.2. Proper Orthogonal Decomposition

Proper orthogonal decomposition (POD) is a robust and efficient method to capture the dynamic structure of the flow. This method extracts an orthogonal basis for the decomposition of a given set of velocity fields. POD has its own roots in statistical analysis and it is developed by Pearson (1901) over hundred years ago. Recently, POD is applied to a flow problem in turbulence by Lumley (1970). This approach has been discussed in details in many publications such as Manhart & Wengle (1993) and Aubry (1991).

POD can be considered as a purely statistical method where the modes are obtained through minimization of the residual energy between the snapshots and their reduced linear representation,

minimize 
$$\sum_{j=0}^{m-1} \| \mathbf{u}(\mathbf{x}_i, t_j) - \sum_{k=0}^{p-1} \phi_{\mathbf{k}}(\mathbf{x}_i) \mathbf{a}_k(t_j) \|_M^2,$$
 subject to  $\langle \phi_l, \phi_k \rangle_M = \delta_{lk} \quad \forall l, k = 0, \dots, p-1.$  (4.3)

where spatial modes  $\mathbf{X} = (\phi_0, \phi_1, \cdots, \phi_k, \cdots, \phi_{m-1})$  are mutually orthogonal and the temporal time coefficients  $\mathbf{a}_k(t_j) = \langle \mathbf{u}_k, \phi_k \rangle_M$  are uncorrelated (Sirovich 1987). This minimization is valid for any number of POD modes  $p \leq m$ . The norm for each  $\mathbf{u}_i, \mathbf{u}_j \in \mathbb{R}^n$  is defined as

$$\langle \mathbf{u}_i, \mathbf{u}_j \rangle_M = \mathbf{u}_i^T \mathbf{M} \mathbf{u}_j \quad \forall \mathbf{u}_i, \mathbf{u}_j \in \mathbb{U}, \text{ and } \| \mathbf{u}_j \|_M^2 = \langle \mathbf{u}_j, \mathbf{u}_j \rangle_M,$$
 (4.4)

where the symbol  $^T$  represents the transpose and  $\mathbf{M} \in \mathbb{R}^{n \times n}$  represents the diagonal spatial weight matrix given by the local cell volumes corresponding to each grid point. A possible solution to this problem is to use the singular value decomposition (SVD) of the weighted snapshot sequence

$$\mathbf{M}^{\frac{1}{2}}\mathbf{U}_{m}\mathbf{N}^{\frac{1}{2}} = \hat{\mathbf{X}}\boldsymbol{\Sigma}\hat{\mathbf{W}}^{T},\tag{4.5}$$

where  $\mathbf{N} \in \mathbb{R}^{n \times n}$  represent the diagonal temporal weight matrix. The columns of  $\hat{\mathbf{X}}$  and  $\hat{\mathbf{W}}$  are the left and right singular vectors, respectively. The matrices  $\hat{\mathbf{X}}$  and  $\hat{\mathbf{W}}$  are unitary  $-\hat{\mathbf{X}}^T\hat{\mathbf{X}} = I$  and  $\hat{\mathbf{W}}^T\hat{\mathbf{W}} = I$ ; here I is the identity matrix. The diagonal entries of  $\Sigma$ , also known as the singular values, are equal to the square root of the eigenvalues of the spatial correlation matrix,  $\Sigma = \hat{\Lambda}^{\frac{1}{2}}$ . The POD modes can be computed as

$$\mathbf{X} = \mathbf{M}^{-\frac{1}{2}}\hat{\mathbf{X}} \tag{4.6}$$

and the temporal coefficients as

$$\mathbf{A} = \mathbf{\Sigma} \mathbf{N}^{-\frac{1}{2}} \hat{\mathbf{W}}. \tag{4.7}$$

The benefit of using POD is the property of its fast convergence to get an accurate reconstruction of the flow with a low number of modes (Frederich & Luchtenburg 2011). On the other hand, since POD extracts an orthogonal basis ranked by their energy content, it is not always easy to interpret the

physical meaning of the spatial modes and their temporal coefficients e.g. in complex flows, different spatial structures and their temporal scales are often present in one mode. In other words, POD allows frequency and scale mixing.

#### 4.3. Dynamic Modal Decomposition

From a mathematical point of view, dynamic modal decomposition (DMD) is an Arnoldi-like method, based on the Koopman operator to analyze data and compute eigenvalues and eigenvectors of an approximate linear model. Without explicit knowledge of the dynamical operator, it extracts frequencies, growth rates, and their related spatial structures (modes). DMD splits the flow into different modes that independently oscillate at a certain frequency. Rowley et al. (2009) presented the theoretical basis of the dynamic mode decomposition to compute the Koopman expansion from a finite sequence of flow fields (snapshots); Schmid (2010) among other considerations, provided an improvement towards a more stable implementation of the DMD algorithm. To compute DMD, we consider a sufficiently long, but finite time series of snapshots (see equation 4.1). We assume a linear mapping that associate the flow field  $\mathbf{u}_j$  to the subsequent flow field  $\mathbf{u}_{j+1}$  such that

$$\mathbf{u}(\mathbf{x}_i, t_{j+1}) = \mathbf{u}_{j+1} = e^{\tilde{\mathbf{A}}\Delta t} \mathbf{u}_j = \mathbf{A}\mathbf{u}_j. \tag{4.8}$$

Hence, it is possible to write

$$\mathbf{u}(\mathbf{x}_i, t_j) = \sum_{k=0}^{m-1} \phi_k(\mathbf{x}_i) \mathbf{a}_k(t_j) = \sum_{k=0}^{m-1} \phi_k(\mathbf{x}_i) e^{\omega_k j \Delta t} = \sum_{k=0}^{m-1} \phi_k(\mathbf{x}_i) \lambda_k^j, \quad (4.9)$$

where  $\omega_k$  and  $\lambda_k$  are the eigenvalues of the matrices  $\tilde{A}$  and A, respectively, and  $\phi_k$  are the corresponding eigenvectors. We also have the relation

$$\lambda_k = e^{\omega_k \Delta t}. (4.10)$$

It is further possible to write  $\phi_k = \mathbf{v}_k d_k$  where  $\| \mathbf{v}_k \|_M = 1$ . We define  $d_k$  as the amplitude and  $d_k^2$  as the energy of the dynamic mode  $\phi_k$ ; the  $\lambda_k$  are associated to the time development of the spatial expansion modes  $\mathbf{v}_k$ . Such an expansion can be interpreted as a finite sum version of the Koopman expansion where the Koopman eigenvalues,  $\lambda_k$ , dictate the growth rate and frequency of each mode (Rowley *et al.* 2009). Without pursuing further, it is sufficient to state that the Koopman expansion puts the dynamic mode decomposition on a firm theoretical foundation.

Equation 4.9 can be rewritten in a matrix form as

$$\mathbf{U}_{m} = \begin{bmatrix} \mathbf{v}_{0}, \mathbf{v}_{1}, \cdots, \mathbf{v}_{m-1} \end{bmatrix} \begin{pmatrix} d_{0} & 0 & \cdots & 0 \\ 0 & d_{1} & \cdots & 0 \\ \vdots & \vdots & \ddots & \vdots \\ 0 & 0 & \cdots & d_{m-1} \end{pmatrix} \begin{pmatrix} 1 & \lambda_{0} & \cdots & \lambda_{0}^{m-1} \\ 1 & \lambda_{1} & \cdots & \lambda_{1}^{m-1} \\ \vdots & \vdots & \ddots & \vdots \\ 1 & \lambda_{m-1} & \cdots & \lambda_{m-1}^{m-1} \end{pmatrix}$$
$$= \tilde{\mathbf{X}} \mathbf{D} \mathbf{S} = \bar{\mathbf{X}} \mathbf{S}. \quad (4.11)$$

where S is a so-called Vandermonde matrix and dictates the time evolution of the dynamic modes. Note that for simplicity, we already incorporated the amplitudes matrix D into  $\bar{X}$ .

To compute the DMD modes  $\bar{\mathbf{X}}$ , we proceed as follows. As the number of snapshots increases, it is reasonable to assume that beyond a certain limit, the snapshot matrix becomes linearly dependent. In other words, adding additional flowfield  $\mathbf{u}_j$  to the data set will not improve the rank of snapshot matrix  $\mathbf{U}_m$ . Hence, one can obtain the flow field sequence  $\mathbf{U}_{m+1} = [\mathbf{u}_1, \cdots, \mathbf{u}_m]$  by a linear combination of the previous snapshot sequence  $\mathbf{U}_m$ . This step is expressed as

$$\mathbf{U}_{m+1} = \mathbf{U}_m \mathbf{C} + \epsilon \mathbf{e}^{\mathbf{T}}, \tag{4.12}$$

where  $\mathbf{e} = [0, \dots, 0, 1]^T$  and  $\boldsymbol{\epsilon}$  contains the residual. This procedure will result in the low-dimensional system matrix  $\mathbf{C}$  which is of companion-matrix type and can be computed using a least square technique (Rowley *et al.* 2009). The matrix  $\mathbf{C}$  can be diagonalized as,

$$\mathbf{C} = \mathbf{S}^{-1} \mathbf{\Lambda} \mathbf{S} = \mathbf{T} \mathbf{\Lambda} \mathbf{T}^{-1}, \quad \mathbf{\Lambda} = \operatorname{diag}(\lambda_1, \dots, \lambda_m),$$
 (4.13)

where  ${\bf S}$  is the Vandermonde matrix and  ${\bf T}$  is the eigenvector matrix using proper scaling so that

$$\mathbf{T} = \mathbf{S}^{-1}\mathbf{D}^{-1}.\tag{4.14}$$

The (diagonal) amplitude matrix  $\mathbf{D}$  will be derived later. The eigenvalues of  $\mathbf{C}$ , collected in  $\mathbf{\Lambda}$ , are also referred to as the Ritz values and approximate some of the eigenvalues of the full nonlinear system. The dynamic modes,  $\bar{\mathbf{X}}$ , are given by

$$\bar{\mathbf{X}} = \mathbf{U}_m \mathbf{S}^{-1} = \mathbf{U}_m \mathbf{T} \mathbf{D} = \tilde{\mathbf{X}} \mathbf{D}, \tag{4.15}$$

where  $\tilde{\mathbf{X}} = \mathbf{U}_m \mathbf{T}$  contain the modal structures. This method is mathematically correct but practical implementation might yield a numerically ill-conditioned algorithm (Schmid 2010). This is especially the case when the data set are rather large and noise contaminated. An improvement to this algorithm was proposed by Schmid (2010), where a self-similar transformation of the companion matrix  $\tilde{\mathbf{C}}$  is obtained as a result of the projection of the velocity fields on the subspace spanned by the corresponding POD modes. The preliminary step of the algorithm is to perform the singular value decomposition of the velocity field sequence. The singular value decomposition of the snapshots (with no weights) results in

$$\mathbf{U}_m = \mathbf{X} \mathbf{\Sigma} \mathbf{W}^T. \tag{4.16}$$

Using this singular value decomposition the self similar transformation of the companion matrix  $\tilde{\mathbf{C}}$  is defined as

$$\tilde{\mathbf{C}} = \mathbf{\Sigma} \mathbf{W}^T \mathbf{C} \mathbf{W} \mathbf{\Sigma}^{-1}. \tag{4.17}$$

The transformed companion matrix  $\tilde{\mathbf{C}}$ , related to  $\mathbf{C}$  via this transformation, is a *full* matrix which improves the conditioning of eigenvalue problem. By computing an optimal companion matrix using equations 4.12 and 4.16 and rearranging equation 4.17, we obtain

$$\tilde{\mathbf{C}} = \mathbf{X}^T \mathbf{M} \mathbf{U}_{m+1} \mathbf{W} \mathbf{\Sigma}^{-1} = \mathbf{Y} \mathbf{\Lambda} \mathbf{Y}^{-1}. \tag{4.18}$$

where  $\mathbf{Y} = (\mathbf{y_1}, \dots, \mathbf{y_m})$  is the eigenvector matrix with  $\mathbf{y}_k^T \mathbf{y}_k = 1 \quad \forall k = 0, \dots, m-1$ . Moreover, the eigenvalues of  $\tilde{\mathbf{C}}$  are the same as for  $\mathbf{C}$ , while their eigenvectors are related by

$$\mathbf{T} = \mathbf{W} \mathbf{\Sigma}^{-1} \mathbf{Y}. \tag{4.19}$$

The modal structures  $\tilde{\mathbf{X}}$  are extracted from the transformed companion matrix  $\tilde{\mathbf{C}}$  in the following way,

$$\tilde{\mathbf{X}} = \mathbf{U}_m \mathbf{T} = \mathbf{U}_m \mathbf{W} \mathbf{\Sigma}^{-1} \mathbf{Y} = \mathbf{X} \mathbf{\Sigma} \mathbf{W}^T \mathbf{W} \mathbf{\Sigma}^{-1} \mathbf{Y} = \mathbf{X} \mathbf{Y}.$$
 (4.20)

It is important to note that the norm  $\| \cdot \|_M$  of the columns of  $\tilde{\mathbf{X}}$  is unity. To obtain the amplitudes of the DMD modes without inverting the Vandernmode matrix  $\mathbf{S}$ , we benefit from the fact that  $\mathbf{D}$  is a diagonal complex matrix. Combining equations 4.15, 4.16 and 4.20, we obtain

$$\bar{\mathbf{X}} = \mathbf{U}_m \mathbf{S}^{-1} = \mathbf{X} \mathbf{\Sigma} \mathbf{W}^T \mathbf{S}^{-1} = \tilde{\mathbf{X}} \mathbf{D} = \mathbf{X} \mathbf{Y} \mathbf{D} \implies \mathbf{D}^{-1} = \mathbf{S} \mathbf{W} \mathbf{\Sigma}^{-1} \mathbf{Y}.$$
 (4.21)

 $\mathbf{D}$  can now be computed by inverting the diagonal entries of matrix  $\mathbf{D}^{-1}$ . Note that equation 4.19 gives a correct scaling for the matrix  $\mathbf{T}$ , thereby combining equations 4.19 and 4.21, one can confirm that the original definition for matrix  $\mathbf{T}$ , equation 4.14, is satisfied.

#### CHAPTER 5

#### Stability of the tip vortices behind a wind turbine

#### 5.1. Mutual inductance instability

The wake behind a wind turbine consists of distinct tip and root vortices. The organised system of vortices are usually unstable and due to different instability mechanisms they break down and forms small scale turbulent structures. Understanding the physical nature of the vortices and their dynamics in the wake of a turbine is, thus, important for the optimal design of a wind farm. In the following the main results from Paper1 will be presented.

A numerical investigation on the wake behind the Tjæreborg wind turbine has been conducted to study the stability properties of the tip vortices and mutual induction instability mechanism. The numerical model is based on large-eddy simulations of the Navier-Stokes equations using the actuator line method. A steady-state simulation is performed to obtain the basic flow behind the wind turbine (figure 5.1(a)). Afterwards, the wake is perturbed by imposing low-amplitude stochastic excitations in the neighbourhood of the blade tips. The amplification of waves traveling along the helix trigger some modes, leading to instability growth and wake breakdown (figure 5.1(b-c)). Depending on the grid configurations and the excitation type, the symmetric and asymmetric conditions are dictated; the symmetric condition is imposed either by confining the polar computational grid to 120° or by introducing the similar type of perturbation (correlated excitation). The uncorrelated excitations for each blade (360° computational grid) imposes an asymmetric condition in the computations. The main objective is to find the underlying mechanism of the onset of tip vortex instability, therefore dynamic mode decomposition (DMD) and proper orthogonal decomposition (POD) are applied in a part of the domain. This subdomain is positioned in a region where the perturbation development is linear and the magnitude of the perturbation velocity remains small compared to the basic flow.

Note that the presence of hub and tower are not considered in the present study; in addition, it is assumed that no interaction between root and tip vortices occurs.

Figure 5.2 shows the DMD spectrum where the amplitude of each mode is plotted against its Strouhal number. The Strouhal number is defined as

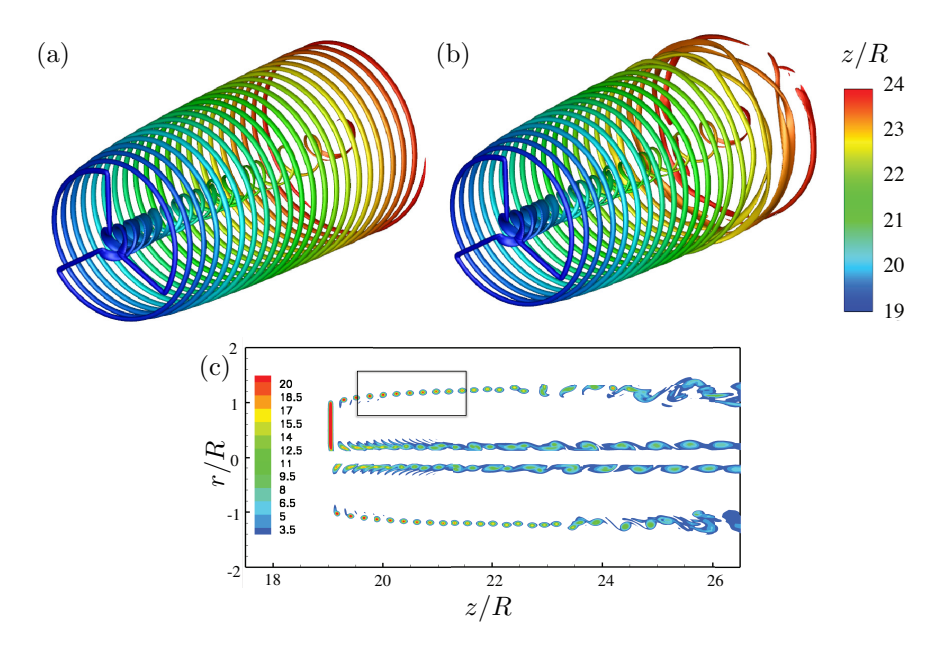
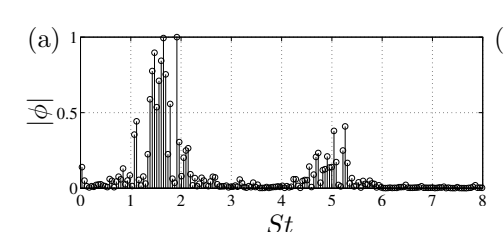


FIGURE 5.1. Isosurfaces of vorticity magnitude colored by axial position. (a) Basic steady state (base flow) and (b) helical vortices break down under the influence of the stochastic noise excitation. (c) Contours of vorticity magnitude in a r-z plane show the development of the tip spiral instability. The black box marks the radial and axial lengths of the subdomain where the modal decomposition techniques are applied.

 $St = fR/U_0$  where R is the blade radius and  $U_0$  is the free-stream velocity. It is observed that a specific group of modes have higher DMD amplitude implying that these modes are involved in the onset of instability. Two group of modes  $St \approx \{2,5\}$  are identified in symmetric setup while four extra modes  $S_t \approx \{0.5,3,4,6\}$  in addition to the symmetric modes are present in the asymmetric configuration. The asymmetric modes are depicted in figure 5.3. Based on the mode shape, it is possible to define the wavelength, K, for any specific mode. Here, K is defined as the number of complete waves over a 360° turn along the spiral. The wavenumber associated to the asymmetric modes are  $K \approx \{1/2, 3/2, 5/2, 7/2, 9/2\}$ . The results from POD analysis are not presented here as similar conclusions can be drawn from POD analysis.

By analysing the disturbance velocity of the dominant modes, it is observed that two velocity (radial and axial) components are larger than the azimuthal one. In addition, there is a  $180^{\circ}$  phase shift between radial and axial velocity which means that there is an out-of-phase relationship between the waves of



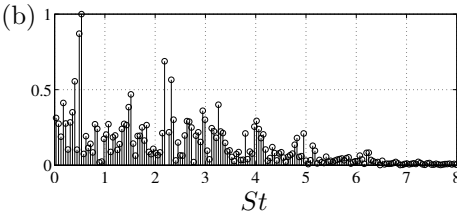


FIGURE 5.2. DMD spectrum for (a) symmetric and (b) asymmetric conditions.

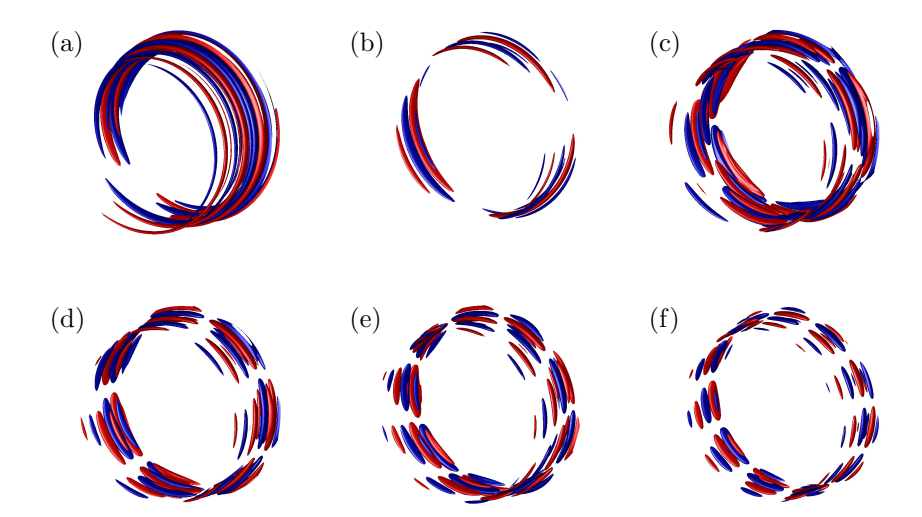


Figure 5.3. Selected dynamic modes of the asymmetric configuration, 360° polar domain, a) first group  $K\approx 1/2,\,St=0.51$  b) second group  $K\approx 3/2,\,St=2.22$  c) third group  $K\approx 5/2,\,St=3.16$  d) fourth group  $K\approx 7/2,\,St=3.90$  e) fifth group  $K\approx 9/2,\,St=4.84$  and f) sixth group  $K\approx 11/2,\,St=6.21$ .

consecutive spirals, (see figure 5.4). This relationship means that if one follows a fluid element along a spiral as it moves in the positive radial direction, it also moves in the negative axial direction and vice versa. This mechanism is called mutual inductance (vortex pairing) which is the primary cause of the wind turbine wake destabilization.

A closer look at the velocity components of the dynamic modes indicate the presence of a wave-like motion, propagating along the spirals. Following

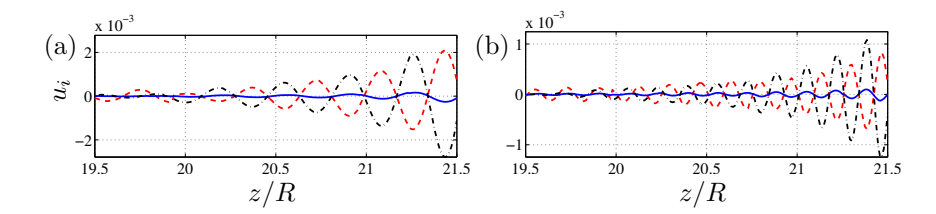


FIGURE 5.4. Amplitude of the velocity components of asymmetric modes. a)  $K \approx 1.5$ ,  $St \approx 2$  and b) $K \approx 4.5$ ,  $St \approx 5$ . The solid, dashed, dashed-dot lines represent the tangential, radial and axial velocity components, respectively.

the perturbation amplitude along the spiral, it can be observed that the perturbations amplify exponentially. The perturbation amplitude is obtained by computing the maximum energy along the spiral at each z-position, i.e. in the flow direction,

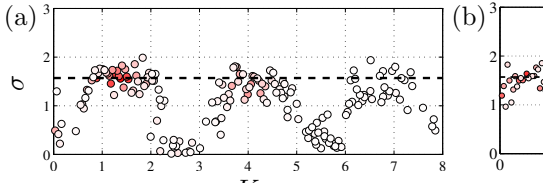
$$w(z) = \max \sqrt{u_r^2 + u_\theta^2 + u_z^2}, \quad r, \theta, z \in \text{spiral trajectory},$$
 (5.1)

where  $u_r$ ,  $u_\theta$  and  $u_z$  are the real value of the radial, azimuthal and axial velocities of the modes. It is now possible to extract the spatial growth rate for each DMD modes by obtaining the slope of the maximum energy curve in the logarithmic scale

$$\tilde{\sigma} = \frac{\mathrm{d}(\log(w/U_c))}{\mathrm{d}z},\tag{5.2}$$

where  $U_c$  is the convective velocity. The obtained spatial growth can be normalized using the distance between vortices h and the circulation  $\Gamma$ . In this case the normalized growth rate can be defined as  $\sigma = \tilde{\sigma}(2h^2U_c/\Gamma)$ . The nondimensional growth rates for the 300 leading DMD modes are reported in figure 5.5. In the symmetric setup, the growth rates follows a sinusoidal type of variation, where the most dominant dynamic modes are the most spatially unstable ones, while in the asymmetric setup all the modes have positive growth rates with a slightly decreasing trend. These results imply that if the excitations are introduced truly randomly in the wind turbine wake, the underlying flow physics is not necessarily the same as the symmetric setup and more modes are involved in the process of tip vortex instability. In other words, the symmetric setup introduces an unphysical limit into the flow problem. The results also suggest that the pairing instability has a maximum universal growth rate equal to  $\pi/2$ . Previous investigations of Levy & Forsdyke (1927); Widnall (1972); Lamb (1932); Leweke et al. (2013); Ivanell et al. (2010) also confirmed the same value.

This investigation shows that amplifications of specific waves along the spiral is responsible for triggering the instability leading to vortex breakdown. The presence of unstable modes in the wake is directly related to the mutual



spond to  $\sigma = \pi/2$ .

K K K K FIGURE 5.5. Spatial growth rate as function of wave number for a) symmetric, 120° polar domain and b) asymmetric configurations. Circles correspond to the DMD modes and they are coloured based on their DMD amplitudes from red (high amplitude) to white (low amplitude). The dashed lines corre-

inductance (vortex pairing) instability where there is an out of phase relation between the waves on the consecutive spirals. In addition, it is found that the mutual inductance instability has a universal growth rate equal to  $\pi/2$ .

#### CHAPTER 6

# Model for determining the stable wake length

Inside a wind farm, it is important to determine the optimum distance between the wind turbines, since closely-spaced wind turbines result in an increased fatigue loads for the interior turbines, whereas too-long-distance between the turbines results in additional installation costs. Therefore, understanding the features influencing the wake structure and the wake length is important in optimal design of wind farms. In the following, the main results from Paper1 and Paper2 will be presented which is a continuation of the work conducted by Ivanell  $et\ al.\ (2010)$ .

In this study, a similar numerical approach as section 5 is followed. First, the basic flow is obtained through steady-state simulation, then small harmonic perturbations are imposed as body force in the neighbourhood of the tip vortices. The frequency of the perturbations as well as their amplitude are varied and the results are subsequently evaluated using Fourier analysis. The amplitude of the perturbations are computed as explained in equation 5.1. Figure 6.1 is a semi-logarithmic plot showing the amplitude development of perturbations with St=2 and St=5 for different perturbation amplitudes. We can identify a linear amplification phase where the perturbation grows exponentially followed by a nonlinear phase in which the perturbation amplitude saturates and nonlinear effects start to become important (Walther et al. 2007). The results show that the growth rate is independent of the initial perturbation amplitude as different data follows the same slope in the linear region. It also depicts that larger initial amplitude leads to an earlier vortex breakdown. Based on the exponential amplification of the perturbations, it is now possible to present

$$A(t) = A_0 e^{\tilde{\sigma}z} = A_0 e^{\tilde{\sigma}U_c t}, \tag{6.1}$$

where  $A_0$  is the initial amplitude at location  $z_0$  and t denotes time. Following the stability analysis in section 5, it is found that the non-dimensional growth rate of mutual inductance instability has a universal value of  $\pi/2$ , so

$$\sigma = \tilde{\sigma} \frac{2h^2 U_c}{\Gamma} = \pi/2 \Rightarrow \tilde{\sigma} = \frac{\pi\Gamma}{4h^2 U_c}.$$
 (6.2)

This expression shows that the growth rate is related to the strength  $(\Gamma)$  and mutual distance (h) of the tip vortices. It is, however, practical to express this equation using the parameters related to operational conditions of a wind

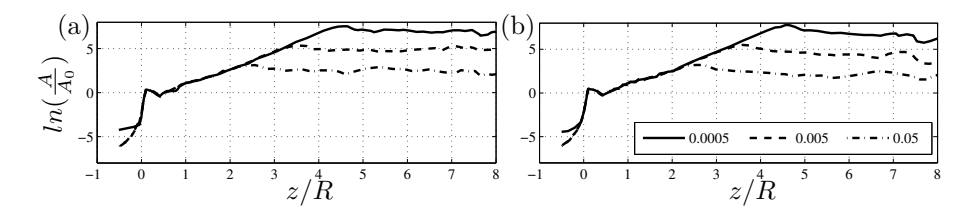


FIGURE 6.1. The development of perturbation amplitude for (a) St=2 and (b) St=5. The values are normalized by the reference value at z=0.5 and the rotor is located at z=0. The legend indicates different initial perturbation amplitudes. The figure is reproduced from Ivanell  $et\ al.\ (2010)$ .

turbine. To accomplish this, some basic results from momentum theory is exploited. Here the vortex model introduced by Okulov & Sørensen (2007) is applied. In their model, it is assumed that the vortex system behind a wind turbine consists of three tip vortices each one with strength  $\Gamma$  and a single root vortex of strength  $-N_b\Gamma$  where  $N_b$  is the number of blades. We can derive the following geometrical relationship:

$$\frac{N_b h}{2\pi R} = \frac{U_c}{\Omega R} \Rightarrow h = \frac{2\pi R U_c}{N_b \lambda U_0}, \tag{6.3}$$

where  $\lambda$  is the tip speed ratio and  $\Omega$  is the rotational frequency. Sørensen & van Kuik (2011) commented that the thrust force can be approximated by

$$T = \frac{1}{2}\rho R^2 \Omega N_b \Gamma, \tag{6.4}$$

if we assume that the rotor blades are loaded with a constant circulation and neglecting the influence of nonlinear rotational terms. The next step is to introduce the thrust coefficient  $C_T=2T/\rho\pi R^2 U_0^2$  and combining equations (6.1)-(6.4) yields

$$\left(\frac{z}{R}\right) = \frac{16\widetilde{U}_c^3}{N_b \lambda C_T} \ln \left(\frac{A(z)}{A_0}\right),\tag{6.5}$$

where  $\widetilde{U}_c = U_c/U_0$ . This expression determines the streamwise position of a given amplitude amplification for a specific operating condition of the wind turbine.

#### 6.1. Length of stable wake

The breakdown position of tip vortices is assumed to take place at the end of linear phase where the perturbation amplitude reaches its maximum. Based on this, it is possible to identify the stable wake length  $(L_{st})$  which is the distance between the rotor plane and the position where the tip vortices starts to breakdown. Ivanell *et al.* (2010) reported that the nonlinear phase

starts when the amplification reaches the ratio between original perturbation and the undisturbed velocity, e.g.

$$\frac{A_{max}(t)}{A_0} \approx \frac{U_0}{u'}. \tag{6.6}$$

It is assumed that the amplitude of the perturbation is proportional to the turbulence intensity  $(T_i)$  with a proportionality constant  $C_1$ ,

$$\frac{u'}{U} = C_1 T_i, (6.7)$$

It is now possible to arrive at the final expression for stable wake length by inserting equations 6.6-6.7 into equation 6.5,

$$\left(\frac{L_{st}}{R}\right) = \frac{-16\tilde{U}_c^3}{N_b \lambda C_T} \ln(C_1 T_i).$$
(6.8)

The two unknown parameters ( $U_c$  and  $C_1$ ) should be calibrated using wind turbine data either from experiments or from simulations. The minus sign in the expression appears due to the fact that the turbulence intensity is always less than one, and the natural logarithmic as a consequence is always negative. This expression gives a measure of the position where the helical tip vortices break down as a function of the intensity of the ambient turbulence level and parameters depending uniquely on the operational characteristics of the turbine.

#### CHAPTER 7

## Interaction of wind turbine wakes

In a wind farm, the interior turbines often operate in the wake of upstream turbines. These turbines are exposed to non-uniform velocity and turbulence intensities significantly higher than the freestream. The velocity deficit reduces the power production and the increased turbulence intensity results in high fatigue loads. Better understanding of the wake aerodynamics in a wind farm requires focusing on fundamental approaches such as wind tunnel investigations under controlled conditions or numerical simulations.

Recently, series of rotor experiments have been carried out at NTNU wind tunnel  $(1.8\times2.7m^2)$  using horizontal axis model scale (D=90cm) rotors, in order to investigate the aerodynamic behaviour of wind turbines. Three different arrangements are studied: a single turbine configuration, two inline turbines where a turbine operates in the wake of an upstream turbine and two turbines with spanwise offset which results in half wake interaction. This chapter reports the numerical investigations conducted based on the NTNU measurements, and summarizes the main results presented in Paper3, Paper4 and Paper5.

### 7.1. Experimental investigation of the NREL S826 airfoil

In NTNU experiment, the wind turbine blades consist of 14% thick NREL S826 airfoil along the span, operating at an effective sectional Reynolds number around Re= $10^5$ . However, prior measured 2D characteristics on the airfoil has only been reported at Re= $10^6$  and above. Here, the sectional Reynolds number is defined as

$$Re_c = \frac{U_{rel}c}{\nu},\tag{7.1}$$

where c is the chord length at a specific radius along the blade and  $\nu$  is the kinematic viscosity. Therefore, a measurement campaign of the airfoil is undertaken in order to obtain the airfoil characteristics at low Reynolds numbers. A 2D blade is manufactured by CNC milling in aluminium with 100mm chord and 499mm span. The airfoil is then mounted vertically in an open loop wind tunnel. The wind tunnel has a cross section of  $500 \times 500mm^2$  with the turbulence intensity of less than 0.2%. The tunnel is equipped with the force balance, wake-rake and a turntable controlled by an electric motor for accurate setting of the blade's angle of attack. The lift force is measured by an acceptable accuracy through the force balance and the drag is determined through

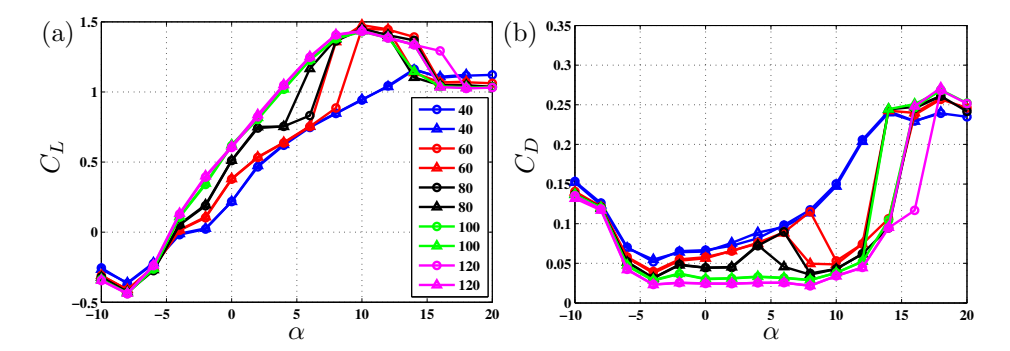


FIGURE 7.1. Measured (a) lift and (b) drag coefficient distributions of NREL S826 without wind tunnel boundary corrections. The circles show the measured data at increasing incidences whereas the triangles are obtained at the decreasing incidences. The values in the caption are Reynolds numbers and they are reported in  $10^3$ .

the integration of wake deficit. The experiments are conducted at five different Reynolds numbers, Re=[40,000 60,000 80,000 100,000 120,000]. The lift and drag coefficients are measured at the period of 30 seconds for each angle of attack stepping with increments of  $2^{\circ}$  from  $-10^{\circ}$  to  $20^{\circ}$  and then to  $-10^{\circ}$ . In this case, both increasing and decreasing angle of attacks are covered to document any aerodynamic hysteresis.

The airfoil characteristics for different Reynolds numbers are presented in figure 7.1. It is observed that the increase in Reynolds number results in higher lift and lower drag coefficients in the linear lift region ( $-4^{\circ} < \alpha < 10^{\circ}$ ). Another observation is that the blade is subjected to hysteresis connected with the onset of laminar separation bubble near the leading edge, affecting the linear part of the lift curve. Higher lift and lower drag values are obtained at increasing incidences whereas, the lower lift and higher drag coefficients are measured at decreasing incidences. The measured lift and drag distributions are then corrected for wind tunnel boundary conditions and the reported data in figure 3.3 are used as an input for the rotor computations presented in next sections.

## 7.2. Setup A: Single model wind turbine

The first part of investigation focuses on the single wind turbine configuration. Numerical computations are performed to predict the performance and wake development behind the turbine. The main goal is to validate the numerical approach, specially testing the new measured 2D airfoil data through comparison with the experimental data. Two numerical approaches are considered, standard blade element momentum (BEM) approach to give an estimation of the

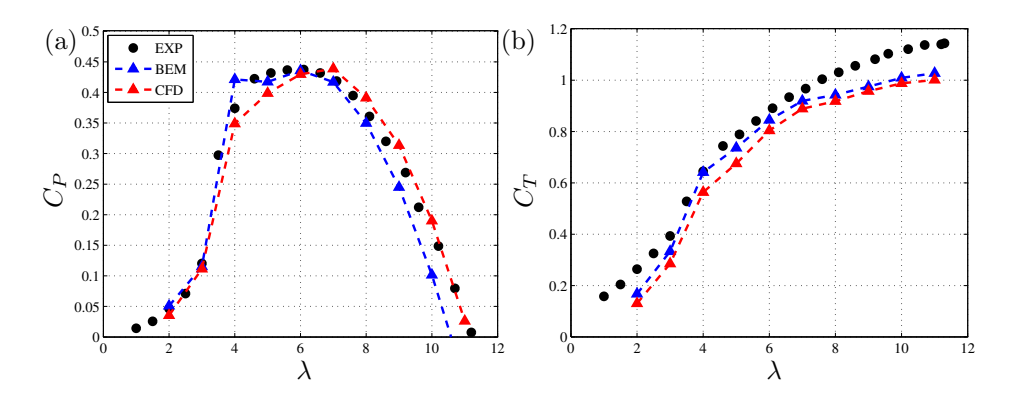


FIGURE 7.2. a) Power and b) thrust coefficients of the single model wind turbine.

rotor performance and CFD computations which are based on the large eddy simulations together with the actuator line technique for the detailed study on the wake development.

The wind turbine is tested inside a wind tunnel which has a 11.2m test section. The cross section of the tunnel is  $1.85 \times 2.71m^2$ . The wind tunnel has a turbulence intensity around  $T_i = 0.23\%$ . The rotor is positioned at 8.2R from the wind tunnel inlet and it has a diameter of 0.894m. The rotor swept area covers almost 12% of the tunnel cross section, therefore, it is expected that the wall interference effects alter the rotor performance. The rotational velocity of the rotor is controlled by an electric motor and is varied from  $\Omega = 10.5$  to  $249 \ rad/s$  which is equivalent to tip speed ratio between  $\lambda = 0.5$  to around 12 based on the freestream velocity. Similar to the test model in the wind tunnel the calculations are performed from  $\lambda = 2$  up to the point where the negative power productions are obtained e.g.  $\lambda = 11$ . The performance of the single wind turbine is presented in figure 7.2. For a wind turbine, the power coefficient is defined as the ratio between the mechanical power of the rotor and the kinetic energy of the wind,

$$C_P = \frac{P}{\frac{1}{2}\rho A U_0^3}. (7.2)$$

The thrust coefficient is also defined as the ratio between the thrust force and the dynamic pressure in the wind,

$$C_T = \frac{T}{\frac{1}{2}\rho A U_0^2},\tag{7.3}$$

where A is the rotor swept area. It should be noted that due to high wind tunnel blockage the BEM results are corrected using an approach suggested by Sørensen  $et\ al.\ (2006)$ . In CFD approach no corrections are needed as the presence of the walls are included in the computations.

It can be observed that the power coefficient increases with the tip speed ratio, reaches a maximum value at the design point ( $\lambda = 6$ ) and then decreases with further increase in the tip speed ratio. There is a drop in power curve when the tip speed ratio falls below  $\lambda = 4$ . This is directly related to the sudden onset of stall (Krogstad & Lund 2011) and with further decrease in tip speed ratio the blade operates in deep stall over the entire span. At very high tip speed ratios  $\lambda > 11$  the inboard section of the blade operates at negative angle of attack results in negative power production. The thrust coefficients show a steady increase with increase of the tip speed ratio. The power coefficients predicted by BEM and CFD approaches follow the same trend as experiment. The BEM calculation, however, under-predicts the power coefficients at high tip speed ratios,  $\lambda > 8$ . This shows that the estimated blockage corrections should be larger than what is already applied in the post-processing of the data. Looking at the thrust coefficients, it is observed that the thrust coefficients are consistently under-predicted by both BEM and CFD methods, specially in offdesign tip speed ratios.

Three tip speed ratios of  $\lambda = 3$ , 6 and 10 are selected for detailed study of the rotor aerodynamic behaviour. The streamwise development of the wake is studied by extracting horizontal profiles after the rotor at specific positions e.q.at x/R = 10.2, 14.2 and 18.2, equivalent to 2R, 6R and 10R behind the rotor, respectively. Figure 7.3 reports the mean velocity and streamwise turbulence stress profiles computed inside the wake. The predicted velocity profiles are generally in agreement with the experiments. The shape of the profiles are correctly predicted; however, small differences can be observed specially near the wake centre due to absence of the hub in the simulations. It can be observed that there are disagreements for the turbulence stress profiles close to the rotor. This is directly related to the actuator line approach where the boundary layer over the blade is not resolved; therefore the presence of small scale structures generated from flow separation over the wing is absent. Further downstream, the turbulence generated from breakdown of the tip and root vortices increase the turbulence level in the predictions in such a way that the predictions match the experimental measurements e.g. in figure 7.3(b,d). A disagreement is observed for the streamwise turbulence stress at the tip speed ratio of  $\lambda=10$ .

In conclusion, it is found that the general shape of power and thrust coefficients are correctly predicted by both methods. However, the thrust coefficients are under-predicted. The velocity profiles are closely matched to the experimental data while some difficulties are observed in matching the turbulence stress.

### 7.3. Setup B: Two inline model wind turbines

In this section, the wake interaction between two modelled wind turbines are studied. The turbines are separated by streamwise distance of  $\Delta x/R = 6$  and

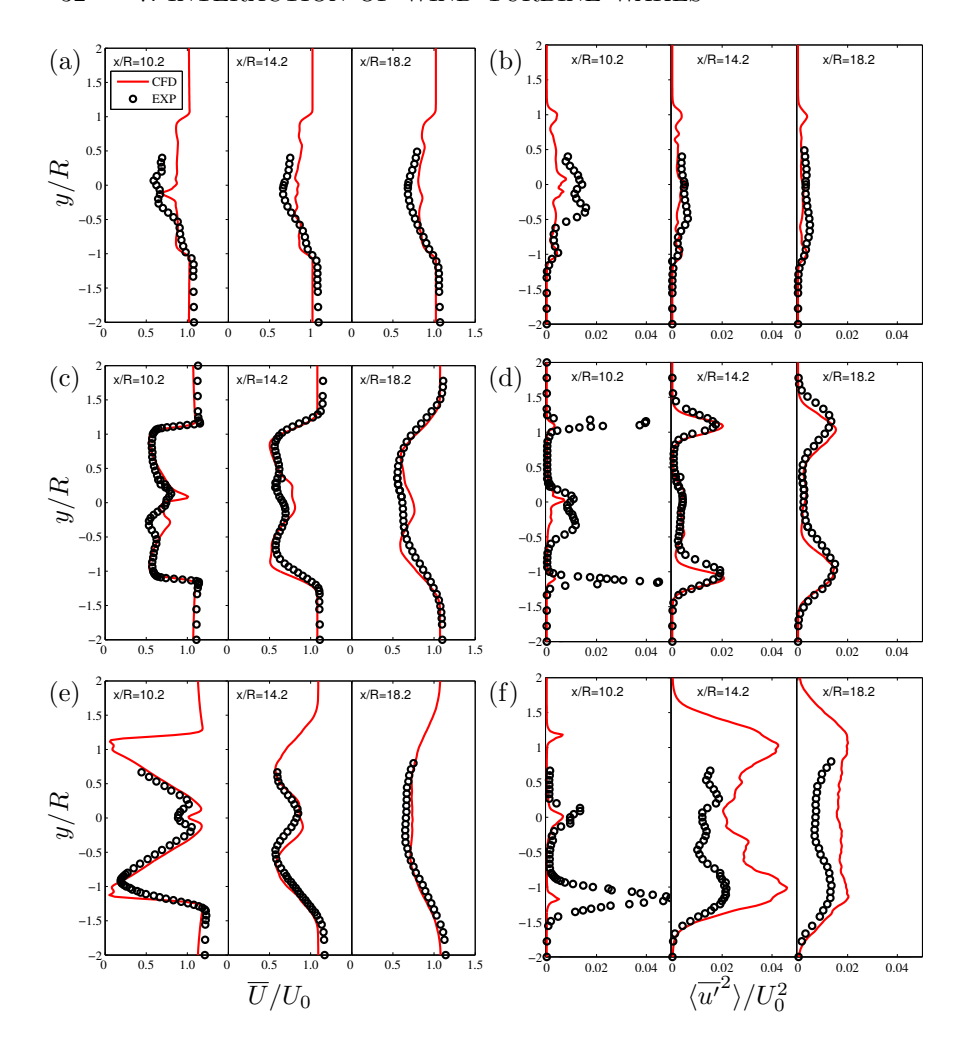


FIGURE 7.3. Wake development behind the single model wind turbine. (a,c,e) show mean velocity profiles  $\overline{U}/U_0$  computed along horizontal line through the rotor center while (b,d,f) are the streamwise turbulent stress  $\langle \overline{u'}^2 \rangle/U_0^2$  computed along horizontal line through the rotor center. (a-b)  $\lambda=3$ , (c-d)  $\lambda=6$  and (e-f)  $\lambda=10$ . The uncertainties in measurements of the mean velocity and streamwise turbulence stress are estimated to be less than  $\pm 2\%$   $U_0$  and  $\pm 6\%$   $U_0^2$ , respectively.

they are positioned in such a way that the full wake interaction scenario happens. Both turbines are equipped with similar blades, but they have different

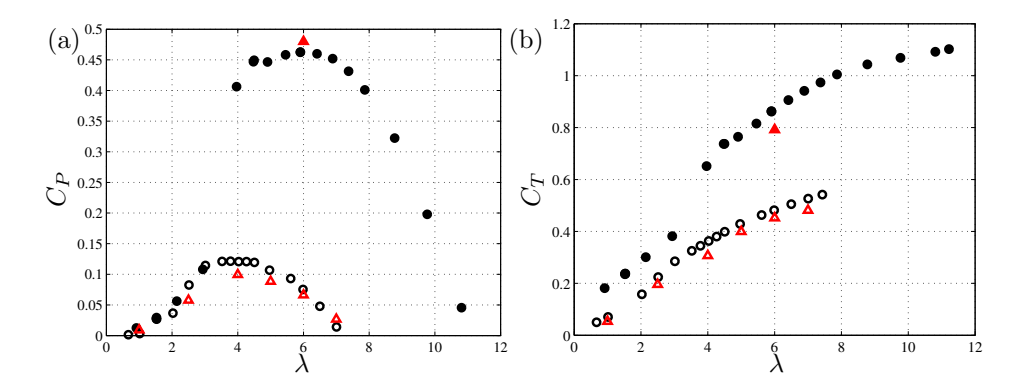


FIGURE 7.4. a) Power and b) thrust coefficients of the two model inline wind turbines. The measurements are presented as the black circles and the computations as the red triangles. The filled symbols indicates the upstream model turbine and the open symbols for the downstream one.

hub and tower geometries. The first rotor is positioned at x/R=4. The upstream wind turbine is set to operate at tip speed ratio  $\lambda_1=6$  and the tip speed ratio of the downstream rotor is varied from  $\lambda_2=0.6$  up to  $\lambda_2=7.4$  where the power production becomes negative. The effect of the interacting wake on the downstream rotor is presented in figure 7.4. It should be mentioned that the coefficients for the downstream turbine is estimated using the freestream velocity at the wind tunnel inlet. A general reduction in the power production and thrust level can be observed as the downstream turbine exposes to a velocity field relatively lower than the upstream one. It can be observed that the general shape of the power and thrust coefficients are correctly predicted. There are however, some difficulties in predicting the power productions around optimum tip speed ratio, where there is almost 20% error in the power coefficient prediction. The thrust coefficients are under predicted for  $\lambda_2 > 2$ .

Three different tip speed ratio of  $\lambda_2=2.5,4$  and 7 are considered for wake development study, where the turbine operates in the deep stall, optimum and run-away conditions, correspondingly. Similar to the single wind turbine, mean velocity and streamwise turbulence stress in three positions (x/R=12,15 and 18) are extracted and they are reported in figure 7.5. It is observed that the overall shape of the wake downstream of the inline configuration has some similarities with the single wind turbine, but due to further extraction of energy by the second wind turbine the velocity deficit is higher than the single turbine. It is observed that the profiles are symmetric and the velocity profiles are top-hat shaped close to the rotor which reach a bell shaped (Gaussian profile) further downstream. The two distinct peaks presented in the streamwise turbulent stress indicates the position of the tip vortices which are smoothed as we move

further downstream. It can also observed that the predicted profiles are in good agreement with the measurements at all tip speed ratios.

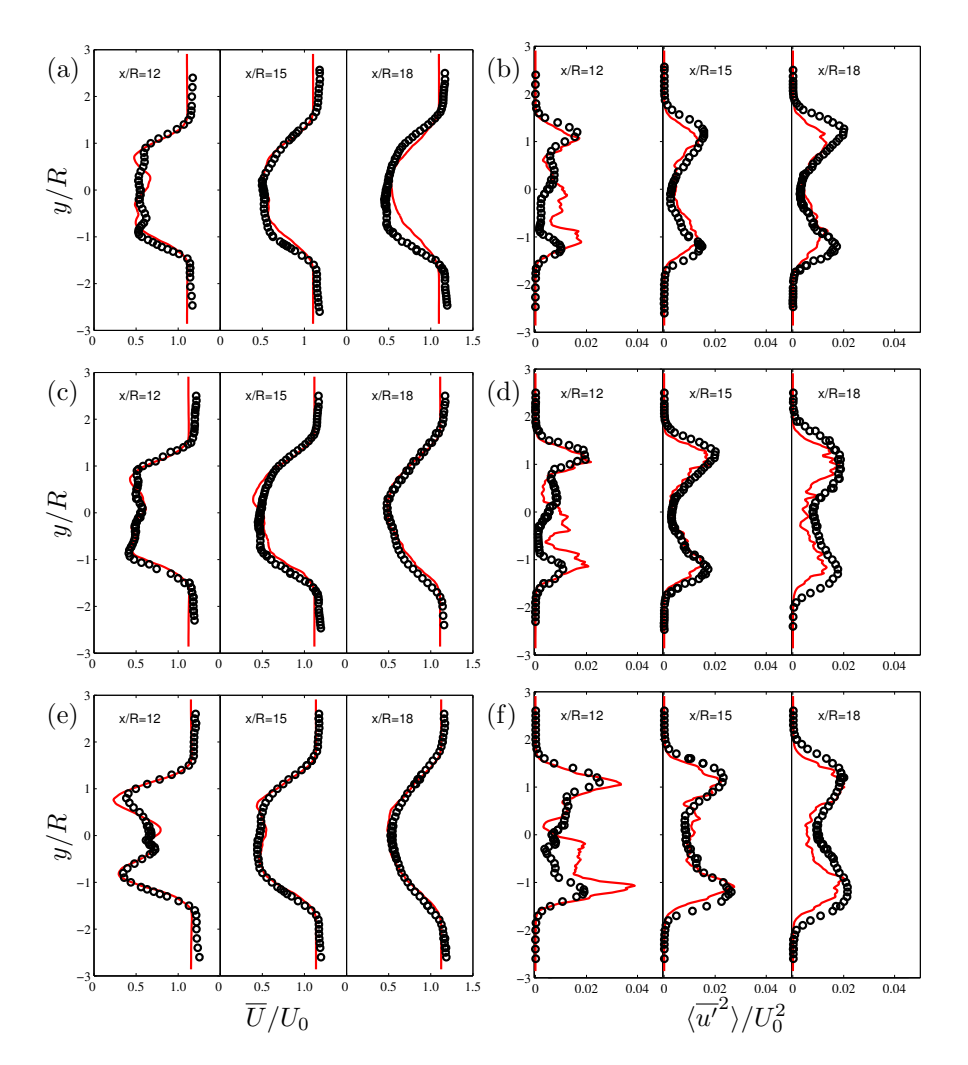


FIGURE 7.5. Wake development behind two inline model wind turbines. (a,c,e) show mean velocity profiles  $\overline{U}/U_0$  computed along horizontal line through the rotor center while (b,d,f) are the streamwise turbulent stress  $\langle \overline{u'}^2 \rangle/U_0^2$  computed along horizontal line through the rotor center. (a-b)  $\lambda_2=2.5$ , (c-d)  $\lambda_2=4$  and (e-f)  $\lambda_2=7$ . The uncertainties in measurements of the mean velocity and streamwise turbulence stress are estimated to be less than  $\pm 4.6\%$   $U_0$  and  $\pm 5.9\%$   $U_0^2$ , respectively.

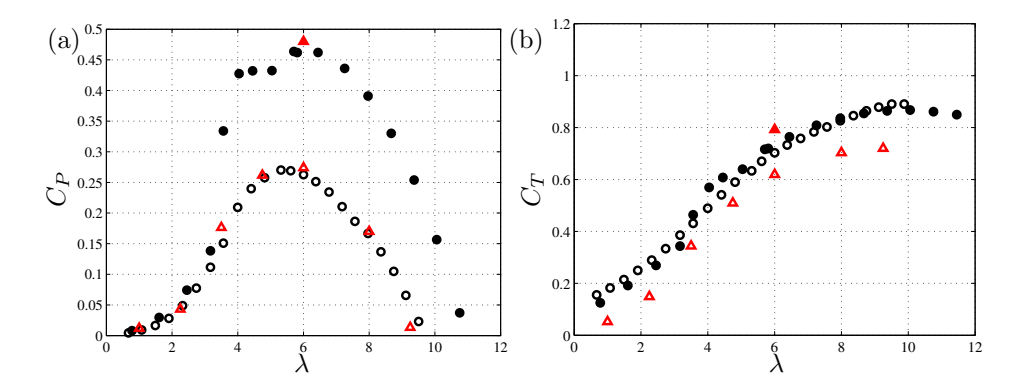


FIGURE 7.6. a) Power and b) thrust coefficients of the two model wind turbines with spanwise offset.

#### 7.4. Setup C: Two model wind turbines with spanwise offset

In this setup, two modelled wind turbines are aligned with a streamwise separation of  $\Delta x/R=6$  and spanwise shift of  $\Delta y=0.9R$ . The rotors are positioned in such a way that the projected area of the upstream rotor covers half of the downstream turbine, resulting in half wake interaction. The model turbines and the wind tunnel turbulence intensity are the same as what are used in section 7.3. The upstream turbine is set to operate at tip speed ratio  $\lambda=6$  and we change the tip speed ratio of the downstream turbine. There is an additional study of the wind turbine wake interaction at high incoming turbulence which is not presented here and we refer to  $Paper\ 5$  for further discussions.

The performance envelope of the turbines are presented in figure 7.6. It can be observed that the power production of the downstream rotor increases as compared to the full wake interaction setup (more than twice at the optimum point). This is due to the fact that the second turbine is partially exposed to higher velocity than the full interaction setup, therefore more energy is available to extract. The tip speed ratio where the power production becomes negative is shifted from  $\lambda \approx 7$  to  $\lambda \approx 10$ . The thrust force applied on the downstream rotor is also increased in comparison with the full wake interaction. The thrust coefficients for the upstream and downstream turbines are approximately the same at  $\lambda = 6$ , implying that a similar physical force is applied to both rotors, although the available energy for the downstream rotor is reduced. The thrust coefficient of the upstream rotor is predicted well by the numerics, while the thrust level of the downstream rotor is under-predicted at all tip speed ratios.

To investigate the wake properties, the wake development behind the second turbine for three different tip speed ratios are reported in figure 7.7. It can be observed that both prediction and experiments produce asymmetric wake.

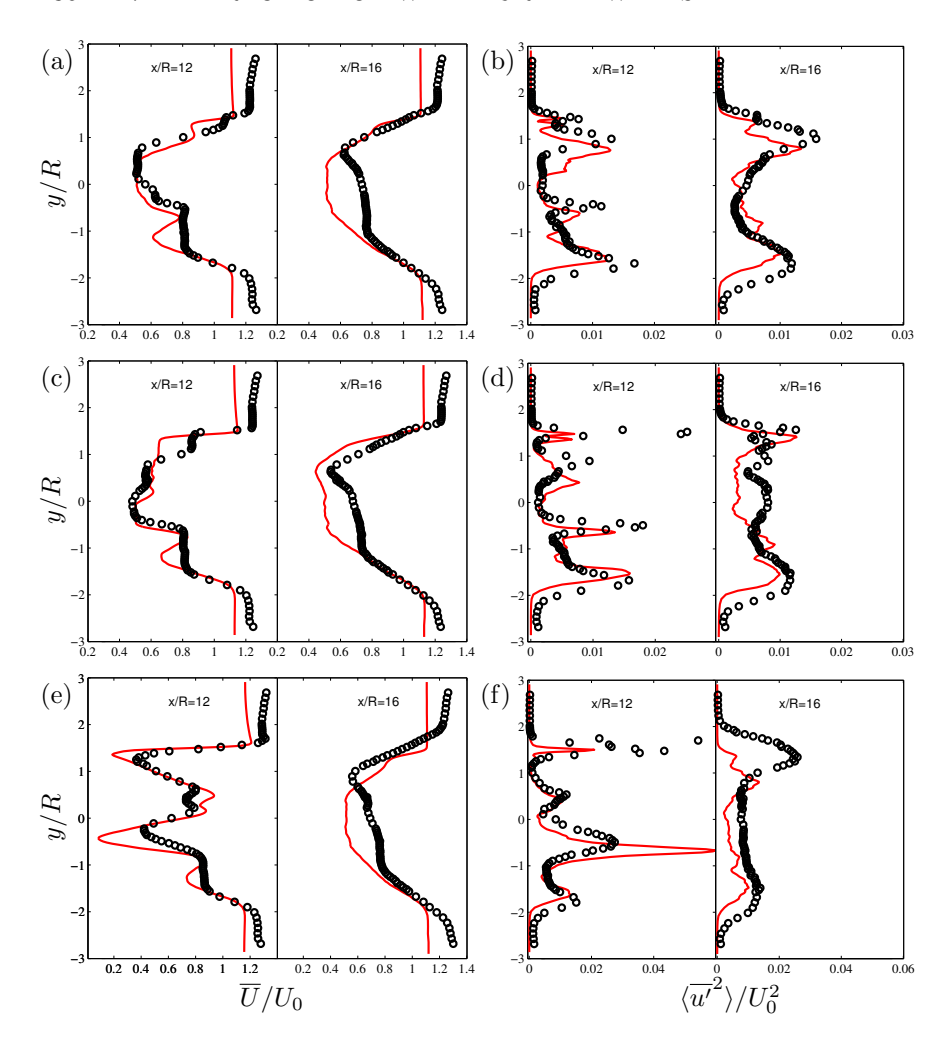


FIGURE 7.7. Wake development behind two model wind turbines with spanwise offset. (a,c,e) shows mean velocity profiles  $\overline{U}/U_0$  computed along horizontal line through the rotor center while (b,d,f) are streamwise turbulent stress  $\langle \overline{u'}^2 \rangle/U_0^2$  computed along horizontal line through the rotor center. (a-b)  $\lambda=3$ , (c-d)  $\lambda=6$  and (e-f)  $\lambda=10$ . The uncertainties in measurements of the mean velocity and streamwise turbulence stress are estimated to be less than  $\pm 2\%~U_0$  and  $\pm 6\%~U_0^2$ , respectively.

Close to the rotor, the wake profile consists of three regions, the two edge regions where the profile is formed purely from the wakes generated by either

downstream or upstream turbines and the centre part which is blend of the two wakes. The turbulent profile is characterized by four distinct peaks generated from the breakdown of the tip vortices. Far downstream, the velocity profiles start to reach the gaussian shape and those peaks in the turbulence stress profiles are smoothed by the spanwise turbulence diffusion. In conclusion, the wake shape and the position of the tip vortices inside the wake are correctly predicted and the observed discrepancies can be related to absence of the hub and the difference in the thrust coefficients.

Based on the provided comparisons, it is demonstrated that the computations based on large eddy simulation together with the actuator line technique can be a complementary tool for investigation of the wind turbine wake interaction.

#### CHAPTER 8

# Near-wake comparison between ACL and vortex model

The growth of wind energy around the world are associated with increased research efforts to improve the comprehension of wind turbine aerodynamics. Many studies are designed for simple calculations and their main focus is to capture the rotor characteristics, e.g. power and thrust coefficients. However, the key point in wind farm optimization is the correct estimation of the flow around the wind turbines. In Paper6 a fast and reliable vortex model is presented and it is investigated whether the predictions of this model can be a substitute of more expensive CFD approach like actuator line technique.

The flow around a single wind turbine is calculated using a vortex model (VM) based on the Biot-Savart law with constant circulation along the blades. The VM is a free-wake vortex model that determines the wake structure from the knowledge of few parameters such as tip speed ratio, number of blades, vortex core size and circulation. The model, without prescribing the wake structure, allows the wake expansion and the free displacement of the tip vortices. This model represents a generalization of the Joukowsky approach. The details about the vortex model is presented in *paper6*.

The model is compared with the actuator line approach in terms of the rotor performance as well as near-wake structure. Two different wind turbines are simulated using both methods: one wind turbine with constant circulation along the blades, to replicate the VM approximations, and the Tjæreborg wind turbine to compare the outcomes of the vortex model with real operative wind turbine conditions.

In order to perform the VM calculations, it is needed to estimate the vortex size and an average circulation for each tip speed ratio. These parameters are obtained from ACL computations e.g. the average circulation along the blade is computed in the range between  $0.2 \le r/R \le 0.9$  that is weakly affected by root and tip effects. In constant circulation setup the forces along the actuator lines are evaluated manually, while for Tjæreborg wind turbine the forces are obtained from the tabulated airfoil data.

Table 8.1 reports the list of input parameters for VM approach together with an estimation of the power and thrust coefficients of both methods. The results show good agreements between the two methods specially for constant circulation data. The differences for Tjæreborg turbine is directly related to

Case	λ	Γ	$\delta/R$	$C_{T,ACL}$	$C_{T,\mathrm{VM}}$	$C_{P, ACL}$	$C_{P,\mathrm{VM}}$	$C_{P, exp}$
A	3.21	0.056	0.080	0.176	0.177	0.153	0.164	-
A	5.05	0.126	0.049	0.61	0.63	0.45	0.48	-
A	7.07	0.130	0.033	0.88	0.90	0.55	0.57	-
В	3.21	0.056	0.080	0.135	0.177	0.113	0.164	0.11
В	5.05	0.126	0.049	0.59	0.63	0.39	0.48	0.41
В	7.07	0.130	0.033	0.82	0.90	0.48	0.57	0.49

Table 8.1. Studied configurations. Case A denotes the wind turbine with constant circulation and case B is the Tjæreborg wind turbine.

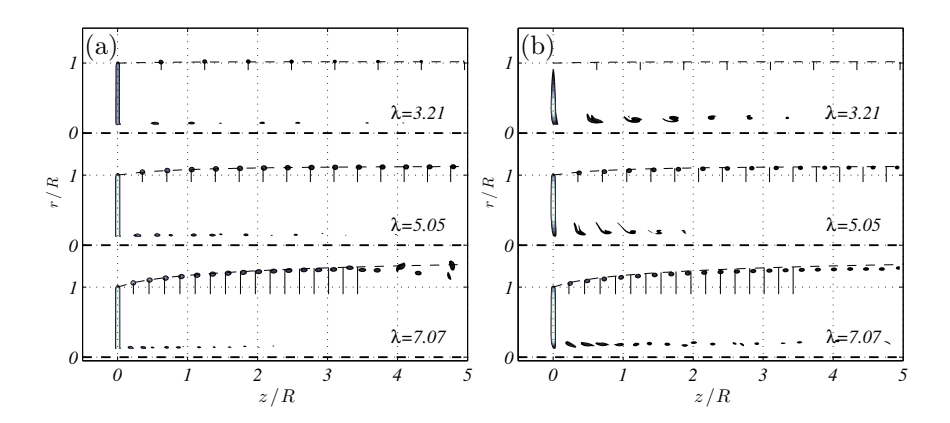


FIGURE 8.1. Azimuthal plane cut at  $\theta = 0^{\circ}$  for (a) the constant circulation wind turbine and (b) the Tjæreborg wind turbine. Contours indicate the vorticity magnitude calculated with the ACL method. The dashed and solid lines indicate the wake envelope and the positions of the vortex cores estimated from the VM, respectively.

the nature of vortex method (irrotational flow assumption) where the effect of the blade drag force is not considered.

A simple indicator of the agreement between the two approaches is provided in figure 8.1 where the wake developments behind the wind turbines are considered. In the constant circulation setup, an excellent agreement between the ACL and the VM is obtained up to z/R=4, a position where the vortex pairing starts to appear in the ACL simulations. In the Tjæreborg setup, changes in the circulation distribution along the blade result in releasing vorticity between the root and tip of the blades leading to the observed discrepancies in the wake envelope. In addition, it can be observed that the ACL vortices

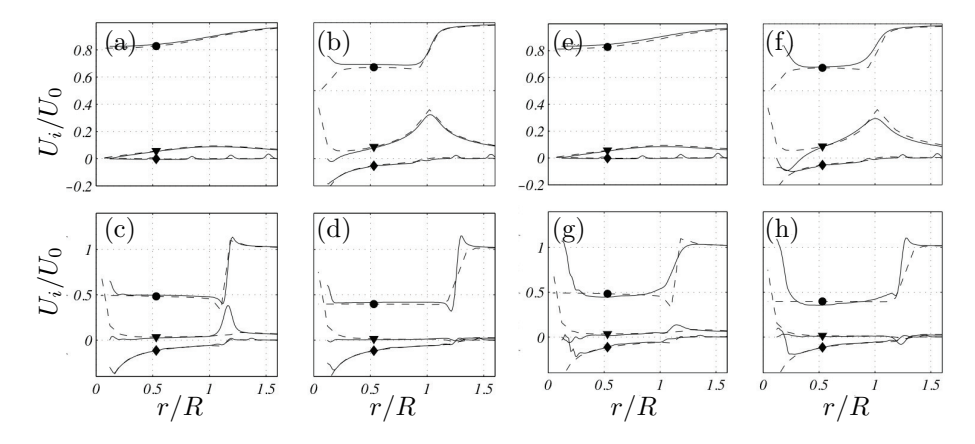


FIGURE 8.2. The velocity component distributions at the streamwise positions (a,e) z/R = -0.5, (b,f) z/R = 0, (c,g) z/R = 1.0 and (d,h) z/R = 3.0. (a-d) present the constant circulation results and (e-h) is the Tjæreborg wind turbine at  $\lambda \approx 7$ . The symbols indicate  $(\bullet)$   $U_z$ ,  $(\blacktriangledown)$   $U_r$  and  $(\blacklozenge)$   $U_\theta$ . Solid lines indicate the ACL results while the dashed lines indicate the VM results.

propagate faster than the vortex model. This comparison shows that the wake development and the wake expansion predicted by the VM agree nicely with the ACL computations.

Figure 8.2 shows the velocity components distributions estimated from both methods. A satisfactory agreement of the velocity components both upstream and at the rotor plane is obtained. Some discrepancies are observed near the tip region where the diffusion mechanisms come into play. The ACL method allows the diffusion of vorticity by viscous actions while the inviscid VM does not allow the smoothing of the strong velocity gradients.

The presented results show that the vortex method is able to qualitatively describe the flow field around the wind turbine; therefore it can be a substitute of more computationally-demanding approach like actuator-line technique.

#### CHAPTER 9

### Conclusions

This project has resulted in an increased knowledge regarding the vortex structures behind wind turbines and interaction of the wind turbine wakes.

In the first part of the project, the stability properties of the tip spiral are studied. The result of the study verified that the amplification of the waves traveling along the tip vortex spirals is associated with an instability leading to wake breakdown and almost all the wave-numbers are involved in the onset of instability. It is found that the mutual inductance instability is the main mechanism behind the tip vortex destabilization and it has a universal growth rate equal to  $\pi/2$ . This project established a new formula to approximate the stable wake length based on the incoming wind turbulence intensity and the operating condition of the wind turbine. This relationship, however, needs to be verified against experiments or numerical data and should be modified in order to take into account the presence of the tower and hub. This formula, if extended to consider the near wake length, can gives us new possibilities to optimize the spacing between turbines inside a wind farm.

This second part verifies that the large eddy simulations using the actuator line method can be a substitute of the experiments to approximate the wind turbine performance and the flow field around the turbines, but with considerable computational cost. It should be noted that reliable tabulated airfoil data is needed to assure the quality of the simulated results.

The third part shows us an alternative cheaper method to study the near-wake flow. Although this method is computationally inexpensive but the application of the vortex method is limited to near-wake study because expanding the model to more general turbine operating states, e.g. wind shear, turbulence, wake interaction results in increase of the method complexity to a level that other models are more attractive.

# Acknowledgments

I would like to acknowledge my main supervisor Prof. Dan S. Henningson for giving me the opportunity to work in his group. Thanks for trusting me as an independent researcher and giving me the opportunity to finish my PhD project.

I would like to thank my co-supervisors Stefan Ivanell and Robert F. Mikkelsen for their help, support and guidance during the project. Many thanks to Robert for sharing his office with me during my stay at DTU and giving me the opportunity to attend the wind car competition. I gratefully acknowledge Prof. Jens N. Sørensen for giving me the opportunity to work in his group. His enthusiasm, trust and invaluable discussions always motivated me and I am really grateful for his guidance during my research. Philipp Schlatter is also acknowledged for his valuable advice and fruitful discussions. I would like to thank Reza Dadfar, Søren J. Andersen and Antonio Segalini for their nice collaborations and helpful discussions. Also, I would like to acknowledge Prof. Per-Åge Krogstad for generously providing the experimental data.

I would like to thank Reza, Azad and Lailai for making our office such an enjoyable place to stay. I really enjoyed the discussions that we had during the lunch time. Many thanks to Azad for proof-reading of the thesis.

I would like to thank all my colleagues in the Nordic Consortium project for Optimization and Control of the wind farms. I would like also to thank the people at KTH Mechanics and DTU Wind Energy that have contributed to a very friendly and pleasant working atmosphere. Many thanks to my friends Armin and Sina for hosting me during my stay in Stockholm and Copenhagen.

Last and not the least, I would like to give special thanks to my family for supporting me all the time specially through the difficult moments. Your contribution to this work is invaluable and countless.

## References

- AINSLIE, J. F. 1988 Calculating the flowfield in the wake of wind turbines. *Journal of Wind Engineering and Industrial Aerodynamics* 27 (1), 213–224.
- Aubry, N. 1991 On the hidden beauty of the proper orthogonal decomposition. Theoretical and Computational Fluid Dynamics 2 (5), 339–352.
- Bennert, W. & Werner, U.-J. 1989 Windenergie (Wind energy). Verlag Technik.
- Elliott, D. 1991 Status of wake and array loss research. In *Presented at the 21st American Wind Energy Association Conference: Windpower 1991, Palm Springs, CA*, 24-27 Sep. 1991, vol. 1, pp. 24-27.
- Frederich, O. & Luchtenburg, D. 2011 Modal analysis of complex turbulent flow. In *Proc. 7th Int. Symp. on Turb. and Shear Flow Phenomena (TSFP-7).*
- GLAUERT, H. 1935 Airplane propellers. Aerodynamic theory 4, 169–360.
- Golding, E. 1976 The generation of electricity by wind power. E.&F.N. Spon Ltd.
- Hansen, M. 2012 Aerodynamics of wind turbines. Routledge.
- HANSEN, M. O. L., SØRENSEN, J. N., VOUTSINAS, S., SØRENSEN, N. & MADSEN, H. A. 2006 State of the art in wind turbine aerodynamics and aeroelasticity. *Progress in aerospace sciences* 42 (4), 285–330.
- IEA 2013a Key world energy statistics. *Tech. Rep.* Technical report, International energy agency.
- IEA 2013b Technology roadmap: Wind energy 2013 edition. *Tech. Rep.* International energy agency.
- IVANELL, S., MIKKELSEN, R., SØRENSEN, J. & HENNINGSON, D. 2010 Stability analysis of the tip vortices of a wind turbine. Wind Energy  ${\bf 13}$  (8), 705–715.
- KROGSTAD, P. & LUND, J. 2011 An experimental and numerical study of the performance of a model turbine. Wind Energy 15 (3), 443–457.
- Lamb, H. 1932  $\it Hydrodynamics, 6th$ edn. Cambridge University Press.
- Levy, H. & Forsdyke, A. 1927 The stability of an infinite system of circular vortices. Proceedings of the Royal Society of London. Series A 114 (768), 594–604.
- Leweke, T., Bolnot, H., Quaranta, U. & Dizès, S. L. 2013 Local and global pairing in helical vortex systems. Int. Conf. on Aerodynamics of Offshore Wind Energy Systems and Wakes, Lyngby, Denmark.
- Lumley, J. L. 1970 Stochastic Tools in Turbulence. Academic Press New York.

- Manhart, M. & Wengle, H. 1993 A spatiotemporal decomposition of a fully inhomogeneous turbulent flow field. *Theoretical and Computational Fluid Dynamics* 5 (4), 223–242.
- Mann, J. 1994 The spatial structure of neutral atmospheric surface-layer turbulence. Journal of Fluid Mechanics 273, 141–168.
- Mann, J. 1998 Wind field simulation. Prob. Engng. Mech 13 (4), 269–282.
- MICHELSEN, J. A. 1992 Basis3d a platform for development of multiblock pde solvers. Tech. Rep AFM 92-06. Dept. of Fluid Mechanics, Technical University of Denmark, DTU.
- MIKKELSEN, R. 2003 Actuator disc methods applied to wind turbines. PhD thesis, Dept. of Fluid Mechanics, Technical University of Denmark, DTU.
- NEUSTADTER, H. & SPERA, D. 1985 Method for evaluating wind turbine wake effects on wind farm performance. *Journal of Solar Energy Engineering* **107** (3), 240–243
- OKULOV, V. L. & SØRENSEN, J. N. 2007 Stability of helical tip vortices in a rotor far wake. J. Fluid Mech. 576 (1), 1–25.
- ØYE, S. 1992 Tjæreborg wind turbine: Dynamic flow measurement. AFM Notat VK 233.
- Pearson, K. 1901 On lines and planes of closest fit to systems of points in space. The London, Edinburgh, and Dublin Philosophical Magazine and Journal of Science 2 (11), 559–572.
- PIERELLA, F., ERIKSEN, P., SÆTRAN, L. & KROGSTAD, P. 2012 Invitation to the 2012" blind test 2" workshop calculations for two wind turbines in line.
- ROWLEY, C., MEZIĆ, I., BAGHERI, S., SCHLATTER, P. & HENNINGSON, D. S. 2009 Spectral analysis of nonlinear flows. *J. Fluid Mech.* **641** (1), 115–127.
- SAGAUT, P. 2005 Large Eddy Simulation for Incompressible Flows An Introduction. New York: Springer.
- Sanderse, B. 2009 Aerodynamics of wind turbine wakes. Energy Research Center of the Netherlands (ECN), ECN-E-09-016, Petten, The Netherlands, Tech. Rep.
- Schepers, J. 2003 ENDOW: Validation and improvement of ECN's wake model. Energy research Centre of the Netherlands ECN.
- Schmid, P. J. 2010 Dynamic mode decomposition of numerical and experimental data. J. Fluid Mech. 656 (1), 5–28.
- SIROVICH, L. 1987 Turbulence and the dynamics of coherent structures. i-coherent structures. ii-symmetries and transformations. iii-dynamics and scaling. *Quart. App. Math.* **45** (1), 561–571.
- SMITH, G., SCHLEZ, W., LIDDELL, A., NEUBERT, A. & PEÑA, A. 1995 Advanced wake model for very closely spaced turbines. *Solar Energy* **54**, 6.
- Somers, D. 2005 The s825 and s826 airfoils. National Renewable Energy Laboratory, Subcontractor Report.
- SØRENSEN, J. 2011a Instability of helical tip vortices in rotor wakes. *Journal of Fluid Mechanics* **682** (1), 1–4.
- SØRENSEN, J. & SHEN, W. 2002 Numerical modeling of wind turbine wakes. *Journal of fluids engineering* 124 (2), 393–399.

- Sørensen, J. N. 2011b Aerodynamic aspects of wind energy conversion. Annual Review of Fluid Mechanics 43, 427–448.
- SØRENSEN, J. N. & VAN KUIK, G. A. M. 2011 General momentum theory for wind turbines at low tip speed ratios. Wind Energy 14 (7), 821–839.
- Sørensen, J. N., Shen, W. Z. & Mikkelsen, R. 2006 Wall correction model for wind tunnels with open test section. AIAA journal  $\bf 44$  (8), 1890–1894.
- SØRENSEN, N. N. 1995 General perpose flow solver applied to flow over hills. PhD thesis, Risø National Laboratory, Roskilde.
- TA Phuoc, L. 1994 Modeles de sous maille appliques aux ecoulements instationnaires decolles. In *Proc. of the DRET conference: 'Aerodynamique Instationnaire Turbulents Aspects Numeriques et Experimentaux*.
- Tangler, J. L., Wohlfeld, R. M. & Miley, S. J. 1973 An experimental investigation of vortex stability, tip shapes, compressibility, and noise for hovering model rotors. *Nat. Aero. and Space Adm.* 2305.
- VERMEER, L. J., SØRENSEN, J. N. & CRESPO, A. 2003 Wind turbine wake aerodynamics. *Progress in Aerospace Science* **39**, 467–510.
- Walther, J., Guenot, M., Machefaux, E., Rasmussen, J., Chatelain, P., Okulov, V., Sørensen, J., Bergdorf, M. & Koumoutsakos, P. 2007 A numerical study of the stability of helical vortices using vortex methods. In *Journal of Physics: Conference Series*, vol. 75, p. 012034. IOP Publishing.
- WIDNALL, S. 1972 The stability of a helical vortex filament. J. Fluid Mech. 4 (54), 641–663